

# Structure of Birnessite Obtained from Decomposition of Permanganate under Soft Hydrothermal Conditions. 1. Chemical and Structural Evolution as a Function of Temperature

Anne-Claire Gaillot,<sup>†</sup> Bruno Lanson,<sup>\*,†</sup> and Victor A. Drits<sup>†,‡</sup>

*Environmental Geochemistry Group, LGIT-Maison des Géosciences, University of Grenoble-CNRS, 38041 Grenoble Cedex 9, France, and Geological Institute, Russian Academy of Sciences, 7 Pyzhevsky street, 109017 Moscow, Russia*

Received January 4, 2005. Revised Manuscript Received March 30, 2005

The structure of a synthetic K-rich birnessite (KBi) prepared by hydrothermally reacting (4 days at 170 °C) a finely ground KMnO<sub>4</sub> powder in acidified water was determined. At room temperature the structure of KBi corresponds to a 3R<sup>-</sup> polytype which can be described as AbC<sub>b</sub><sup>a</sup>CaB<sub>c</sub><sup>a</sup>BcA<sub>b</sub><sup>c</sup>AbC... using the close-packing formalism. Assuming an orthogonal base-centered unit cell, KBi has  $a = b\sqrt{3} = 4.923$  Å,  $b = 2.845$  Å,  $\gamma = 90^\circ$ , and  $c = 21.492$  Å. The layer charge deficit originates exclusively from the presence of vacant layer sites as only Mn<sup>4+</sup> cations are present in the octahedral layers, and the following structural formula can be proposed: K<sub>0.296</sub><sup>+</sup>(Mn<sub>0.926</sub><sup>4+</sup>□<sub>0.074</sub>)O<sub>2</sub>·0.40H<sub>2</sub>O. The layer charge deficit is compensated by the sole presence of interlayer K in prismatic cavities located above (or below) an empty tridentate cavity of the lower (or upper) layer and below (or above) a Mn octahedron of the upper (or lower) layer. This site is shifted from the center of the prismatic cavity toward its faces. This structure is essentially unaffected when heating this sample up to 250 °C, except for the dehydration of KBi interlayers. Heating the KBi sample to 350 °C leads to a dramatic modification of its crystal chemistry resulting from the partial reduction of layer Mn<sup>4+</sup> cations associated with the departure of O<sub>layer</sub> atoms. Despite unfavorable steric strains induced by the Jahn–Teller distortion of Mn<sup>3+</sup>-octahedra, reduced Mn<sup>3+</sup> cations remain in the octahedral layers, leading to vacancy-free layers with the following structural formula: K<sub>0.312</sub><sup>+</sup>(Mn<sub>0.761</sub><sup>4+</sup>Mn<sub>0.215</sub><sup>3+</sup>□<sub>0.024</sub>)O<sub>2</sub>·0.42H<sub>2</sub>O. At 350 °C the partial reduction of Mn<sub>layer</sub> leads to a dramatic increase of the lateral dimensions of the layer arising from the random orientation of the long Mn<sup>3+</sup>–O bond with respect to the **a** axis. After cooling, the structure of KBi becomes monoclinic (space group C2/m) with  $a = 5.130$  Å,  $b = 2.850$  Å,  $c = 7.131$  Å, and  $\beta = 101.0^\circ$ . In this case steric strains are minimized by the segregation of Mn<sup>3+</sup>-octahedra in Mn<sup>3+</sup>-rich rows parallel to the **b** axis and by the systematic orientation of their long Mn–O bonds along the **a** axis. The origin of the above structural modifications and the nature of the stacking disorder are also determined.

## Introduction

Birnessite has a layer structure consisting of edge-sharing MnO<sub>6</sub> octahedra with hydrated cations in the interlayer space compensating for the layer charge deficit which arises either from the coexistence of heterovalent Mn cations within layers or from the presence of vacant layer octahedra.<sup>1–5</sup> This mineral occurs in diverse geological settings including deep-ocean nodules, ore deposits of Mn and other metals, soils, and alteration crusts.<sup>3–19</sup> Although present in limited amounts, birnessite plays a pivotal role in the fate of heavy metals

and other pollutants in contaminated water systems and soils.<sup>18–31</sup> This role originates from its unique cation

\* To whom correspondence should be addressed. E-mail: Bruno.lanson@obs.ujf-grenoble.fr.

<sup>†</sup> University of Grenoble.

<sup>‡</sup> Russian Academy of Sciences.

- (1) Giovanoli, R.; Stähli, E.; Feitknecht, W. *Helv. Chim. Acta* **1970**, *53*, 209–220.
- (2) Giovanoli, R.; Stähli, E.; Feitknecht, W. *Helv. Chim. Acta* **1970**, *53*, 453–464.
- (3) Burns, R. G.; Burns, V. M. *Philos. Trans. R. Soc. London, Ser. A* **1977**, *286*, 283–301.
- (4) Glover, E. D. *Am. Mineral.* **1977**, *62*, 278–285.
- (5) Chukhrov, F. V.; Gorschkov, A. I.; Rudnitskaya, E. S.; Sivtsov, A. V. *Izv. Akad. Nauk Geol.* **1978**, *9*, 67–76.
- (6) Burns, V. M.; Burns, R. G. *Earth Planet. Sci. Lett.* **1978**, *39*, 341–348.

- (7) Golden, D. C.; Dixon, J. B.; Chen, C. C. *Clays Clay Miner.* **1986**, *34*, 511–520.
- (8) Chukhrov, F. V.; Sakharov, B. A.; Gorschkov, A. I.; Drits, V. A.; Dikov, Yu. P. *Int. Geol. Rev.* **1985**, *27*, 1082–1088.
- (9) Drits, V. A.; Petrova, V. V.; Gorschkov, A. I. *Lithol. Raw Mater.* **1985**, *3*, 17–39.
- (10) Cornell, R. M.; Giovanoli, R. *Clays Clay Miner.* **1988**, *36*, 249–257.
- (11) Manceau, A.; Lanson, B.; Schlegel, M. L.; Harge, J. C.; Musso, M.; Eybert Berard, L.; Hazemann, J. L.; Chateigner, D.; Lamble, G. M. *Am. J. Sci.* **2000**, *300*, 289–343.
- (12) Bilinski, H.; Giovanoli, R.; Usui, A.; Hanzel, D. *Am. Mineral.* **2002**, *87*, 580–591.
- (13) Rogers, T. D. S.; Hodgkinson, R. A.; Cronan, D. S. *Mar. Georesour. Geotechnol.* **2001**, *19*, 245–268.
- (14) McKeown, D. A.; Post, J. E. *Am. Mineral.* **2001**, *86*, 701–713.
- (15) Exon, N. F.; Raven, M. D.; De Carlo, E. H. *Mar. Georesour. Geotechnol.* **2002**, *20*, 275–297.
- (16) Mote, T. I.; Becker, T. A.; Renne, P.; Brimhall, G. H. *Econ. Geol. Bull. Soc. Econ. Geol.* **2001**, *96*, 351–366.
- (17) Morozov, A. A.; Novikov, G. V.; Kulikova, L. N. *Geochem. Int.* **2001**, *39*, 764–779.
- (18) Manceau, A.; Tamura, N.; Celestre, R. S.; MacDowell, A. A.; Geoffroy, N.; Sposito, G.; Padmore, H. A. *Environ. Sci. Technol.* **2003**, *37*, 75–80.
- (19) Vaniman, D. T.; Chipera, S. J.; Bish, D. L.; Duff, M. C.; Hunter, D. B. *Geochim. Cosmochim. Acta* **2002**, *66*, 1349–1374.

exchange capacity,<sup>32–36</sup> sorption,<sup>36–48</sup> and redox properties.<sup>21,28,36,45–54</sup>

To study these properties and the reaction mechanisms involved, synthetic birnessite-like structures are most often used as they are easily obtained under laboratory conditions. Recently, synthetic birnessite has attracted additional attention as a potential cathode material for rechargeable batteries, and extensive research is presently carried out to define optimal conditions for the synthesis of a low-cost and

environmentally safe birnessite-like structure to replace the LiCoO<sub>2</sub> cathode commonly used in commercial cells. Birnessite is synthesized either from the oxidation of Mn<sup>2+</sup> in a highly alkaline medium<sup>1,2,10,55</sup> or from the reduction of Mn<sup>7+</sup> using permanganate (MnO<sub>4</sub><sup>−</sup>) as the starting reagent. In the latter case, different protocols have been proposed including mild hydrothermal synthesis,<sup>56–58</sup> sol–gel processes,<sup>59–64</sup> interaction of KMnO<sub>4</sub> with hydrochloric acid followed by a cation exchange,<sup>7,65–67</sup> and thermal decomposition of KMnO<sub>4</sub> or of a MnO–LiOH–KNO<sub>3</sub> mixture at very high temperatures.<sup>55,68–70</sup>

Birnessites obtained by these protocols differ from each other by important structural and chemical features and by their properties. Therefore, to understand the relationships between structure and properties of the different birnessite varieties, a comprehensive crystal chemical study of each variety is required. In the present article and in the companion article structural and chemical features of birnessite samples obtained from the mild hydrothermal treatment of potassium and sodium permanganates are investigated.<sup>71</sup> From the decomposition at 170 °C of KMnO<sub>4</sub> in acidified water this synthesis protocol initially developed by Chen et al. directly leads to a K-birnessite variety with structural formula K<sub>0.25</sub>–MnO<sub>2</sub>·0.6H<sub>2</sub>O.<sup>57,58</sup> These authors concluded that this birnessite variety has a hexagonal layer symmetry, a three-layer periodicity, and crystallizes in space group R $\bar{3}m$ . Using the integrated intensity refinement approach, they also determined an idealized structure model for this K-birnessite variety.<sup>57</sup> However, important details of the actual structure of this hydrothermally synthesized birnessite variety were only partially determined. In particular, atomic positions of the different interlayer species (K<sup>+</sup> cations and H<sub>2</sub>O molecules) were not differentiated. More important, the average oxidation degree of Mn and the origin of the layer charge (coexistence of heterovalent Mn cations and/or presence of vacant layer sites) were not determined. In addition, these

- (20) Chao, T. T.; Theobald, P. K. *Econ. Geol.* **1976**, *71*, 1560–1569.
- (21) Manceau, A.; Drits, V. A.; Silvester, E. J.; Bartoli, C.; Lanson, B. *Am. Mineral.* **1997**, *82*, 1150–1175.
- (22) Manceau, A.; Schlegel, M. L.; Chateigner, D.; Lanson, B.; Bartoli, C.; Gates, W. P. In *Synchrotron X-ray methods in clay science*; Schulze, D. G., Stucki, J. W., Bertsch, P. M., Eds.; Clay Minerals Society: Boulder, CO, 1999; Clay Miner. Soc. Workshop Lectures Vol. 9, pp 68–114.
- (23) Manceau, A.; Lanson, B.; Drits, V. A.; Chateigner, D.; Gates, W. P.; Wu, J.; Huo, D.; Stucki, J. W. *Am. Mineral.* **2000**, *85*, 133–152.
- (24) Manceau, A.; Drits, V. A.; Lanson, B.; Chateigner, D.; Wu, J.; Huo, D.; Gates, W. P.; Stucki, J. W. *Am. Mineral.* **2000**, *85*, 153–172.
- (25) Taylor, R. M.; McKenzie, R. M.; Norrish, K. *Aust. J. Soil Res.* **1964**, *2*, 235–248.
- (26) McKenzie, R. M. *Aust. J. Soil Res.* **1967**, *5*, 235–246.
- (27) McKenzie, R. M. *Aust. J. Soil Res.* **1980**, *18*, 61–73.
- (28) Kim, J. G.; Dixon, J. B.; Chusuei, C. C.; Deng, Y. J. *Soil Sci. Soc. Am. J.* **2002**, *66*, 306–315.
- (29) Cheney, M. A.; Shin, J. Y.; Crowley, D. E.; Alvey, S.; Malengreau, N.; Sposito, G. *Colloid Surf., A* **1998**, *137*, 267–273.
- (30) Mench, M. J.; Manceau, A.; Vangronsveld, J.; Clijsters, H.; Mocquot, B. *Agronomie* **2000**, *20*, 383–397.
- (31) McBride, M. B.; Martinez, C. E. *Environ. Sci. Technol.* **2000**, *34*, 4386–4391.
- (32) Healy, T. W.; Herring, A. P.; Fuerstenau, D. W. *J. Colloid Interface Sci.* **1966**, *21*, 435–444.
- (33) Balistrieri, L. S.; Murray, J. W. *Geochim. Cosmochim. Acta* **1982**, *46*, 1041–1052.
- (34) Gray, M. J.; Malati, M. A. *J. Chem. Technol. Biotechnol.* **1979**, *29*, 127–134.
- (35) Stumm, W. *Chemistry of the solid-water interface and particle–water interface in natural systems*; Wiley: New York, 1992.
- (36) Le Goff, P.; Baffier, N.; Bach, S.; Pereira-Ramos, J.-P. *Mater. Res. Bull.* **1996**, *31*, 63–75.
- (37) Tu, S.; Racz, G. J.; Goh, T. B. *Clays Clay Miner.* **1994**, *42*, 321–330.
- (38) Paterson, E.; Swaffield, R.; Clark, L. *Clay Miner.* **1994**, *29*, 215–222.
- (39) Novikov, G. V.; Cherkashev, G. A. *Geochem. Int.* **2000**, *38 Suppl. 2*, S194–S205.
- (40) Dyer, A.; Pillinger, M.; Harjula, R.; Amin, S. *J. Mater. Chem.* **2000**, *10*, 1867–1874.
- (41) Naidja, A.; Liu, C.; Huang, P. M. *J. Colloid Interface Sci.* **2002**, *251*, 46–56.
- (42) Gray, M. J.; Malati, M. A. *J. Chem. Technol. Biotechnol.* **1979**, *29*, 135–144.
- (43) Catts, J. G.; Langmuir, D. *Appl. Geochem.* **1986**, *1*, 255–264.
- (44) Ran, Y.; Fu, J. M.; Rate, A. W.; Gilkes, R. J. *Chem. Geol.* **2002**, *185*, 33–49.
- (45) Manceau, A.; Gorshkov, A. I.; Drits, V. A. *Am. Mineral.* **1992**, *77*, 1144–1157.
- (46) Manceau, A.; Gorshkov, A. I.; Drits, V. A. *Am. Mineral.* **1992**, *77*, 1133–1143.
- (47) Silvester, E. J.; Manceau, A.; Drits, V. A. *Am. Mineral.* **1997**, *82*, 962–978.
- (48) Manceau, A.; Charlet, L. *J. Colloid Interface Sci.* **1992**, *148*, 425–442.
- (49) Stone, A. T.; Godfredsen, K. L.; Deng, B. In *Chemistry of aquatic systems: Local and global perspectives*; Bidoglio, G., Stumm, W., Eds.; ECSC, EEC, EAEC: Brussels, 1994; pp 337–374.
- (50) Guha, H.; Sainers, J. E.; Brooks, S.; Jardine, P.; Jayachandran, K. *J. Contam. Hydrol.* **2001**, *49*, 311–334.
- (51) Tournassat, C.; Charlet, L.; Bosbach, D.; Manceau, A. *Environ. Sci. Technol.* **2002**, *36*, 493–500.
- (52) Petrie, R. A.; Grossl, P. R.; Sims, R. C. *Environ. Sci. Technol.* **2002**, *36*, 3744–3748.
- (53) Manning, B. A.; Fendorf, S. E.; Bostick, B.; Suarez, D. L. *Environ. Sci. Technol.* **2002**, *36*, 976–981.
- (54) Banerjee, D.; Nesbitt, H. W. *Geochim. Cosmochim. Acta* **1999**, *63*, 1671–1687.
- (55) Kim, S. H.; Im, W. M.; Hong, J. K.; Oh, S. M. *J. Electrochem. Soc.* **2000**, *147*, 413–419.
- (56) Feng, Q.; Kanoh, H.; Miyai, Y.; Ooi, K. *Chem. Mater.* **1995**, *7*, 1226–1232.
- (57) Chen, R. J.; Zavalij, P.; Whittingham, M. S. *Chem. Mater.* **1996**, *8*, 1275–1280.
- (58) Chen, R. J.; Chirayil, T.; Zavalij, P.; Whittingham, M. S. *Solid State Ionics* **1996**, *86–88*, 1–7.
- (59) Bach, S.; Henry, M.; Baffier, N.; Livage, J. *J. Solid State Chem.* **1990**, *88*, 325–333.
- (60) Bach, S.; Pereira-Ramos, J.-P.; Baffier, N. *Electrochim. Acta* **1993**, *38*, 1695–1698.
- (61) Le Goff, P.; Baffier, N.; Bach, S.; Pereira-Ramos, J.-P. *J. Mater. Chem.* **1994**, *4*, 875–881.
- (62) Ching, S.; Landrigan, J. A.; Jorgensen, M. L.; Duan, N.; Suib, S. L.; O’Young, C. L. *Chem. Mater.* **1995**, *7*, 1604–1606.
- (63) Ching, S.; Petrovay, D. J.; Jorgensen, M. L.; Suib, S. L. *Inorg. Chem.* **1997**, *36*, 883–890.
- (64) Cho, J.; Kim, G. B.; Lim, H. S.; Kim, C.-S.; Yoo, S.-I. *Electrochem. Solid-State Lett.* **1999**, *2*, 607–609.
- (65) Tsuji, M.; Komarneni, S.; Tamaura, Y.; Abe, M. *Mater. Res. Bull.* **1992**, *27*, 741–751.
- (66) Leroux, F.; Guyomard, D.; Piffard, Y. *Solid State Ionics* **1995**, *80*, 299–306.
- (67) McKenzie, R. M. *Miner. Magn.* **1971**, *38*, 493–502.
- (68) Herbstein, H. F.; Ron, G.; Weissman, A. *J. Chem. Soc. (A)* **1971**, 1821–1826.
- (69) Kim, S. H.; Kim, S. J.; Oh, S. M. *Chem. Mater.* **1999**, *11*, 557–563.
- (70) Gaillot, A. C.; Flot, D.; Drits, V. A.; Manceau, A.; Burghammer, M.; Lanson, B. *Chem. Mater.* **2003**, *15*, 4666–4678.
- (71) Gaillot, A.-C.; Lanson, B.; Drits, V. A. *Chem. Mater.* **2005**, in preparation.

authors recognized that important issues such as the nature of structural defects in these phyllosulfates needed to be refined. These structural features of K-birnessite are specifically detailed in the present manuscript. In addition, special attention is paid to the structural modifications observed as a function of temperature. Structural modifications of K-birnessite resulting from cation exchange processes are described in the companion paper.<sup>71</sup>

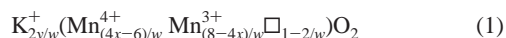
## Experimental Section

**Experimental Methods.** K-birnessite (hereafter referred to as KBi) was prepared by acidifying 0.025 mol of finely ground KMnO<sub>4</sub> in 50 mL of water with 5 drops of 4 M HNO<sub>3</sub>, giving a pH of ~3 and a Mn:H<sup>+</sup> ratio of 100:1.<sup>57</sup> After aging for 1 month in a light-free environment and under constant stirring, the solution was transferred into a 250 mL Teflon-lined autoclave (Paar bomb), sealed, and reacted hydrothermally for 4 days at 170 °C. After reaction, the solution pH was highly alkaline (pH ~ 13). The resulting black crystals were filtered, washed several times with deionized Milli-Q water (18.2 MΩ·cm<sup>-1</sup>), then freeze-dried, and stored under room conditions for further chemical and structural characterizations.

The morphology of KBi particles was observed on a JEOL JSM 6320F high-resolution scanning electron microscope (SEM) equipped with a field-emission electron source.

**Thermal and Chemical Analyses—Structural Formula.** Thermal analysis of KBi was carried out with a NETZSCH Simultan STA 409 EP analyzer. DT-TG data were collected in air using a 10 °C/min heating rate over the 20–1100 °C temperature range to determine the amount of structural water and the temperatures characteristic of structural changes.

Total contents of Mn and interlayer K were determined using a Perkin-Elmer Optima 3000 ICP-AES after digestion of about 8 mg of birnessite powder in 200 mL of a 1% HNO<sub>3</sub>/0.1% NH<sub>3</sub>OH.Cl matrix. The mean oxidation degree of manganese in KBi was determined by potentiometric titration using (NH<sub>4</sub>)<sub>2</sub>Fe(SO<sub>4</sub>) Mohr salt and sodium pyrophosphate.<sup>72,73</sup> The mean oxidation state, 2x, in combination with the atomic ratio y = K/Mn determined from the chemical analyses, allows calculating the structural formula of KBi using the relation<sup>70</sup>



where  $w = (2x + y)/2$  and  $\square$  represents vacant layer site. This structural formula can be refined by taking into account the amounts of interlayer H<sub>2</sub>O molecules deduced from the DT-TG analysis.

**X-ray Diffraction Data Collection.** Powder XRD patterns were recorded using a Bruker D5000 powder diffractometer equipped with a Kevex Si(Li) solid detector and Cu K $\alpha$  radiation. Intensities were recorded from 5 to 80° 2 $\theta$ , using 0.04° 2 $\theta$  steps, and a 40 s counting time per step. A TTK450 Anton Paar chamber was used to record patterns from a KBi sample heated in situ. The initial KBi sample before thermal treatment will be hereafter referred to as sample RoomT-KBi, while 100-KBi, 150-KBi, 250-KBi, and 350-KBi refer to KBi samples heated in situ at 100 °C, 150 °C, 250 °C, and 350 °C, respectively. KBi sample was heated in situ to the desired temperature at a 6 °C/min rate similar to that used for the DT-TG analyses. A 2-h plateau at fixed temperature was observed before starting XRD data collection so that the sample may reach its thermal equilibrium. All KBi XRD patterns from

the temperature series were recorded successively in a single continuous experiment, increasing the temperature stepwise. The AfterT-KBi sample will hereafter refer to the KBi sample after the complete thermal treatment up to 350 °C and subsequent cooling to room temperature.

**Simulation of Powder XRD Patterns.** One of the effective ways to determine the actual structure of defective layered compounds is the calculation of powder XRD patterns using the mathematical formalism described by Drits et al.<sup>74</sup> This trial-and-error fitting procedure has been successfully used to determine the crystal-chemical structure of different natural and synthetic birnessites containing random stacking faults or consisting of the interstratification of different layer types.<sup>8,21,70,75–79</sup> Details on the program used to simulate XRD patterns and on the fitting procedure are given by Plançon and Drits et al.<sup>75,80,81</sup> Specifically, the coherent scattering domains in the layer plane were assumed to have a disklike shape whose radius was adjusted. For each sample, the background was assumed to be linearly decreasing over the angular range. No preferred orientation was considered in agreement with the peculiar geometry of particles clusters revealed by SEM observations. The quality of fit was estimated over the 34–74° 2 $\theta$  Cu K $\alpha$  range using the usual  $R_{wp}$  parameter.

## Results

**Size and Shape of KBi Particles.** SEM observations of KBi samples show that these samples consist of ball-like particles having a 2–5  $\mu$ m diameter (Figures 1a and 1b) as described earlier.<sup>57</sup> A closer look at these ball-like particles reveals that they actually consist of an aggregate of individual platelike crystals that are strongly held together and whose maximum length and thickness are ~1  $\mu$ m and ~20 nm, respectively (Figures 1b and 1c). These crystal shape and dimensions are very similar to those usually reported for natural birnessite crystals or for their synthetic analogues obtained according to various protocols, except for the high-temperature decomposition of KMnO<sub>4</sub> which leads to crystals micrometer-sized along all directions.<sup>70</sup> A layer “crust” covering part of the ball-like aggregates is sometimes observed (Figure 1b). This peculiar morphology of the aggregates likely prevents the preferential orientation commonly observed for other varieties of natural or synthetic birnessites when prepared for powder XRD analysis.

**Loss of Weight during Heating.** Thermogravimetric (TG) analysis of KBi shows four distinct losses of weight labeled a–d in Figure 2a. The two low-temperature losses at ~90 °C and ~140 °C (a and b) are commonly assumed to correspond to adsorbed and interlayer water whereas the one occurring between 250 °C and 400 °C (c) likely corresponds to the loss of oxygen atoms from the octahedral layer

(72) Vetter, K. J.; Jaeger, N. *Electrochim. Acta* **1966**, *11*, 401–419.

(73) Lingane, J. J.; Karplus, R. *Ind. Eng. Chem. Anal. Ed.* **1946**, *18*, 191–194.

(74) Drits, V. A.; Tchoubar, C. *X-ray diffraction by disordered lamellar structures: Theory and applications to microdivided silicates and carbons*; Springer-Verlag: Berlin, 1990.

(75) Drits, V. A.; Lanson, B.; Gorshkov, A. I.; Manceau, A. *Am. Mineral.* **1998**, *83*, 97–118.

(76) Lanson, B.; Drits, V. A.; Silvester, E. J.; Manceau, A. *Am. Mineral.* **2000**, *85*, 826–838.

(77) Lanson, B.; Drits, V. A.; Feng, Q.; Manceau, A. *Am. Mineral.* **2002**, *87*, 1662–1671.

(78) Lanson, B.; Drits, V. A.; Gaillot, A. C.; Silvester, E.; Plançon, A.; Manceau, A. *Am. Mineral.* **2002**, *87*, 1631–1645.

(79) Gaillot, A. C.; Drits, V. A.; Plançon, A.; Lanson, B. *Chem. Mater.* **2004**, *16*, 1890–1905.

(80) Plançon, A. Ph.D. Thesis, Orléans, France, 1976.

(81) Plançon, A. *J. Appl. Crystallogr.* **2002**, *35*, 377.

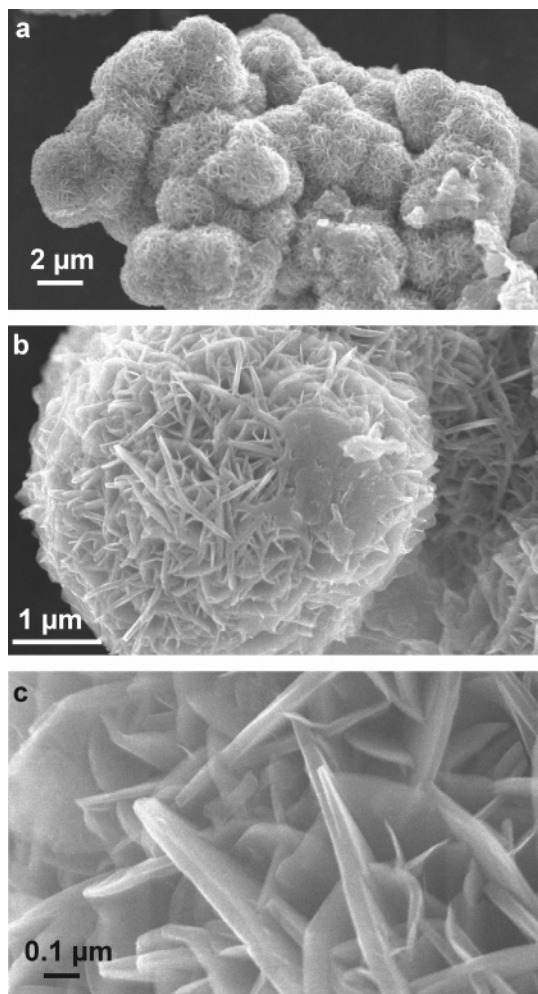
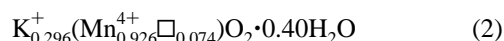


**Figure 1.** Scanning electron micrographs of KBi particles.

framework in relation to the partial reduction of  $\text{Mn}^{4+}$  to  $\text{Mn}^{3+}$ .<sup>57,68</sup> A similar reduction of  $\text{Mn}^{4+}$  to  $\text{Mn}^{3+}$  and loss of structural O anions has been reported for pyrolusite ( $\text{MnO}_2$ ) at  $\sim 350\text{--}400\text{ }^\circ\text{C}$ .<sup>82</sup> Finally, the strong endothermic peak in the DT curve and the associated weight loss at  $\sim 890\text{ }^\circ\text{C}$  (d) is most likely related to the melting of KBi.

For sample AfterT-KBi losses of weight are observed at  $\sim 90\text{ }^\circ\text{C}$ ,  $\sim 165\text{ }^\circ\text{C}$ , and  $\sim 910\text{ }^\circ\text{C}$  (Figure 2b), which correspond to the endotherms a, b, and d, respectively, observed for sample RoomT-KBi. However, in contrast with sample RoomT-KBi, sample AfterT-KBi exhibits a weight gain at  $\sim 320\text{ }^\circ\text{C}$  (c), rather than a weight loss.

**Chemical Analyses and Structural Formula.** For RoomT-KBi the K/Mn atomic ratio ( $y = 0.320$ ) can be calculated from ICP analytical results whereas the  $\text{H}_2\text{O}/\text{Mn}$  ratio (0.43) is deduced from the 7.5% weight loss measured between  $100\text{ }^\circ\text{C}$  and  $220\text{ }^\circ\text{C}$  and corresponding to the loss of structural water. Another 2.7% weight loss is observed over the  $250\text{--}400\text{ }^\circ\text{C}$  range. Before the thermal treatment, the structure of RoomT-KBi contains only  $\text{Mn}^{4+}$  cations as the measured oxidation state of Mn is equal to  $4.00 \pm 0.02$ , and its structural formula can thus be written as



In contrast, the oxidation state measured for Mn in the AfterT-KBi sample is much lower ( $3.78 \pm 0.02$ ), showing

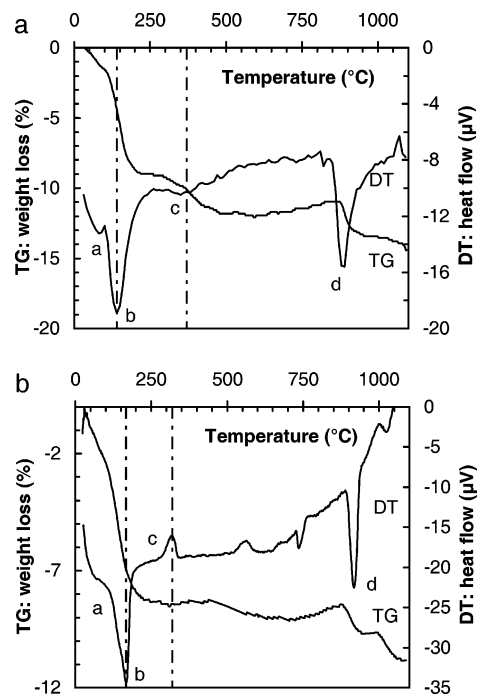
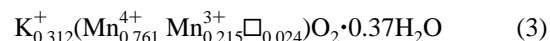


**Figure 2.** Experimental TG and DT curves obtained for samples RoomT-KBi (a) and AfterT-KBi (b). The different endothermic peaks corresponding to successive loss of weight occur at  $\sim 90\text{ }^\circ\text{C}$ ,  $\sim 140\text{ }^\circ\text{C}$ ,  $250\text{--}400\text{ }^\circ\text{C}$ , and  $\sim 890\text{ }^\circ\text{C}$  and are labeled a, b, c, and d, respectively, for sample RoomT-KBi. For sample AfterT-KBi a weight gain rather than a weight loss is observed over the  $250\text{--}400\text{ }^\circ\text{C}$  temperature interval.

that the AfterT-KBi sample contains  $\sim 22\%$  of  $\text{Mn}^{3+}$  and  $\sim 78\%$  of  $\text{Mn}^{4+}$  cations if the relative proportion of  $\text{Mn}^{2+}$  is assumed to be negligible. In addition, the 6.4% weight loss measured between  $100\text{ }^\circ\text{C}$  and  $230\text{ }^\circ\text{C}$  after rehydration corresponds to the loss of structural water. If the K/Mn ratio is unchanged after the rehydration of the heated KBi sample at room temperature, the structural formula of AfterT-KBi can be written as



**Indexing of the Experimental XRD Patterns.** Figure 3 compares the XRD patterns of KBi recorded at room temperature (before and after thermal treatment) and at temperatures ranging from  $100\text{ }^\circ\text{C}$  to  $350\text{ }^\circ\text{C}$ . Following their indexing as described below, experimental and calculated  $d(hkl)$  values are listed in Table 2 for all KBi samples and the corresponding unit-cell parameters are reported in Table 1. Note that Table 1 also contains the unit-cell parameters of additional phases identified in samples 100-KBi, 350-KBi, and AfterT-KBi samples while fitting their respective XRD patterns with the trial-and-error approach described by Drits et al.<sup>74</sup>

**Sample RoomT-KBi.** The XRD pattern of RoomT-KBi can be indexed using a three-layer rhombohedral ( $3R$ ) unit cell having  $a_{\text{th}} = b_{\text{th}} = 2.845\text{ \AA}$ ,  $\gamma = 120^\circ$ , and  $c = 21.492\text{ \AA}$  (space group  $R\bar{3}m$ ) as described by Chen et al.<sup>57</sup> However, for later needs, the indexing was performed systematically with an orthogonal base-centered unit cell having  $a_{\text{ort}} = a_{\text{th}}\sqrt{3} = 4.923\text{ \AA}$ ,  $b_{\text{ort}} = b_{\text{th}} = 2.845\text{ \AA}$ ,  $\gamma = 90^\circ$ , and  $c = 21.492\text{ \AA}$  (Table 1). Going from low- to high-angle values,

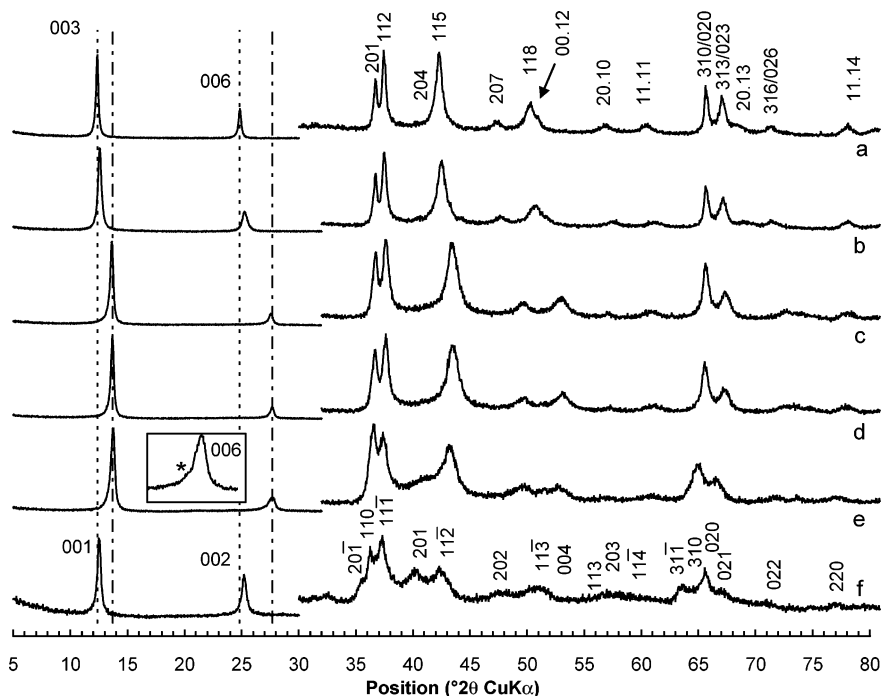


**Figure 3.** Experimental powder XRD pattern obtained for KBi samples. (a) Pattern recorded at room temperature (sample RoomT-KBi). (b) to (e) Patterns recorded in situ at 100 °C, 150 °C, 250 °C, and 350 °C (samples 100-, 150-, 250-, and 350-KBi, respectively). (f) Pattern recorded after the complete thermal treatment up to 350 °C and subsequent cooling to room temperature (sample AfterT-KBi).

**Table 1. Unit-Cell Parameters of KBi Samples as a Function of Temperature**

	polytype	$a^a$	$b^a$	$c^a$	$\beta$
RoomT-KBi	$3R^-$	4.928	2.845	21.492	90°
100-KBi	$3R^-$	4.928	2.845	21.120	90°
				19.380	90°
150-KBi	$3R^-$	4.936	2.850	19.380	90°
250-KBi	$3R^-$	4.938	2.851	19.260	90°
350-KBi	$3R^-$	4.967	2.868	19.206	90°
	$3R^-/3R^+$	4.997	2.885	19.356	90°
AfterT-KBi	$3R^-$	4.971	2.870	21.150	90°
	$1M$	5.130	2.850	7.126	100.8°

<sup>a</sup> Unit-cell parameters are given in Å. <sup>b</sup> Unit-cell parameters of the main quasi-periodic phase. <sup>c</sup> Unit-cell parameters of the  $3R^+/3R^-$  mixed layer phase. <sup>d</sup> Unit-cell parameters of the  $3R^-$  fragments in both the main phase and the quasi-turbostratic phase.

the powder XRD pattern of RoomT-KBi (Figure 3a) contains a rational series of basal reflections with a  $d(003)$  value corresponding to a minimum periodicity of 7.164 Å along the  $c^*$  axis followed by two families of  $hkl$  reflections having for indices (i)  $20l$  ( $l = 3n + 1$ ,  $n$  integer) and  $11l$  ( $l = 3n - 1$ ) over the 34–80°  $2\theta$  range and (ii)  $31l$  and  $02l$  ( $l = 3n$ ) over the 64–80°  $2\theta$  range.

**Heated-KBi Samples.** XRD patterns obtained during heating of KBi sample are very similar to that recorded on the initial RoomT-KBi sample and can also be indexed using  $3R$  unit cells (unit-cell parameters being hereafter expressed in the orthogonal system). Figures 3b–d show that only intense dehydration occurs when heating the sample up to 250 °C, thus inducing a significant decrease of the  $d(003)$  value down to 6.46–6.42 Å and related shifts of nonbasal reflections (Table 2). Figure 4 shows that the decrease of  $c$  parameter is accompanied by a limited increase of  $a$  ( $=b\sqrt{3}$ ) and  $b$  unit-cell parameters (Table 1), the hexagonal layer symmetry being preserved up to that temperature ( $a = b\sqrt{3}$ ,  $\gamma = 90^\circ$ ). In contrast, a dramatic increase of the lateral dimensions of the layer was observed ( $b = 2.868$  Å, Table

1, Figure 4) when heating the sample to 350 °C. A careful examination shows that with increasing temperatures  $00l$  diffraction lines are broadened and that their asymmetry is increased. For example, the tail which is present on the low-angle side of both 003 and 006 reflections above 100 °C results in a shoulder at 350 °C (inset in Figure 3e), thus suggesting the presence of crystals with a larger dimension along the  $c^*$  axis. When the temperature is increased to 350 °C,  $hkl$  reflections are broadened in addition to  $00l$  ones, the profiles of some of these reflections becoming asymmetrical. In addition, for some of these  $hkl$  reflections the mismatch between measured and calculated  $d(hkl)$  values exceeds the experimental error (Table 2). As discussed below, these specific features of experimental XRD profiles are related to the heterogeneous phase composition of sample 350-KBi.

**Sample AfterT-KBi.** Following the thermal treatment up to 350 °C, the XRD pattern recorded at room temperature on sample AfterT-KBi is dramatically modified as compared to those of both RoomT-KBi and 350-KBi. The diffraction pattern can be indexed assuming a one-layer monoclinic unit cell ( $1M$ ) with  $a = 5.130$  Å,  $b = 2.850$  Å,  $c = 7.131$  Å,  $\beta = 101.0^\circ$  (space group  $C2/m$ ). The octahedral layers of AfterT-KBi have thus an orthogonal symmetry with  $a > b\sqrt{3}$  whereas all other samples had a hexagonal layer symmetry. Adjacent layers are shifted with respect to each other by  $c \cos \beta = -0.260a$  along the  $a$  axis, and the basal spacing  $d(001)$  is equal to  $c \sin \beta = 7.000$  Å. As for sample 350-KBi,  $hkl$  reflections of AfterT-KBi have broad and asymmetrical profiles and for some of them a noticeable discrepancy between  $d_{\text{exp}}(hkl)$  and  $d_{\text{cal}}(hkl)$  can be observed (Table 2). It will be shown below that these specific features of experimental XRD profiles are related to the heterogeneous phase composition of sample AfterT-KBi.

Table 2. Indexing of the Experimental XRD Patterns of KBi Samples with 3R and 1M Unit Cells

3R <i>hkl</i> <sup>a</sup>	RoomT		100-KBi		150-KBi		250-KBi		350-KBi		AfterT-KBi		1M <i>hkl</i> <sup>a</sup>
	<i>d</i> <sub>exp</sub> <sup>b</sup>	<i>d</i> <sub>calc</sub> <sup>c</sup>	<i>d</i> <sub>exp</sub>	<i>d</i> <sub>calc</sub>	<i>d</i> <sub>exp</sub>	<i>d</i> <sub>calc</sub>	<i>d</i> <sub>exp</sub>	<i>d</i> <sub>calc</sub>	<i>d</i> <sub>exp</sub>	<i>d</i> <sub>calc</sub>	<i>d</i> <sub>exp</sub>	<i>d</i> <sub>calc</sub>	
003	7.167	7.164	7.039	7.040	6.494	6.468	6.468	6.420	6.437	6.442	7.063	7.000	001
006	3.581	3.582	3.524	3.520	3.234	3.234	3.222	3.210	3.220	3.221	3.529	3.500	002
											2.523	2.526	201
												2.520	200
201	2.446	2.445	2.447	2.445	2.446	2.445	2.449	2.447	2.457	2.465	2.476	2.481	110
112	2.399	2.399	2.398	2.399	2.390	2.391	2.390	2.390	2.404	2.404	2.410	2.409	111
009		2.388		2.347		2.156		2.140		2.147	2.351	2.333	003
204		2.237	2.227	2.231		2.197		2.195	2.200	2.210	2.245	2.255	202
											2.241	2.241	201
115	2.136	2.136	2.126	2.128	2.083	2.082	2.080	2.078	2.096	2.089	2.131	2.118	112
											2.117	2.117	112
											1.962	1.941	112
207	1.919	1.920	1.906	1.908	1.834	1.842	1.832	1.837	1.839	1.847	1.910	1.898	203
118	1.814	1.815	1.797	1.801	1.726	1.730	1.724	1.723	1.736	1.731	1.795	1.784	113
00.12	1.791	1.791	1.765	1.760	1.615	1.617	1.607	1.605	1.614	1.611		1.750	004
20.10	1.615	1.619	1.601	1.603	1.521	1.525	1.514	1.518	1.520	1.526	1.614	1.626	113
											1.567	1.571	203
11.11	1.530	1.530	1.515	1.514		1.435	1.437	1.428	1.436	1.434	1.485	1.465	311
											1.449	1.447	310
310												1.425	020
020	1.421	1.421	1.421	1.422	1.422	1.423	1.423	1.424	1.436	1.434	1.422	1.421	312
313													
023	1.395	1.394	1.394	1.394	1.390	1.390	1.392	1.390	1.403	1.400	1.395	1.396	021
20.13	1.374	1.372	1.363	1.356	1.300	1.294	1.270	1.270	1.319	1.276	1.374	1.374	311
316													
026	1.322	1.321	1.321	1.318	1.300	1.303	1.308	1.302	1.287	1.310	1.328	1.330	313
319													
029	1.224	1.221	1.222	1.221	1.223	1.234	1.221	1.221	1.187	1.221	1.239	1.240	220

<sup>a</sup> All KBi samples are indexed as 3R<sup>-</sup> polytypes (indices in the left-hand side column), except for sample AfterT-KBi which is indexed as a 1M polytype (indices in the right-hand side column). <sup>b</sup> *d*<sub>exp</sub>(*hkl*) are measured experimentally. <sup>c</sup> *d*<sub>calc</sub>(*hkl*) values are calculated using the unit-cell parameters of the main phases listed in Table 1.

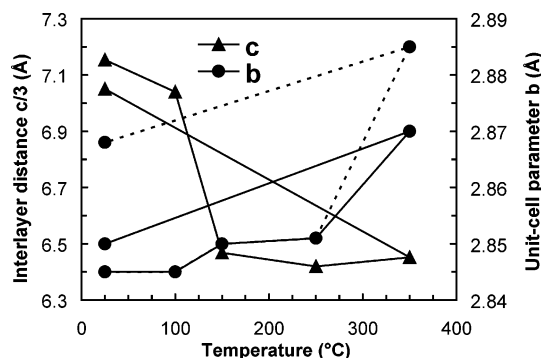


Figure 4. Evolution of unit-cell parameters for KBi samples as a function of temperature. The solid and dashed lines outline the variation of unit-cell parameters in the main ordered structure, and in the accessory structures, respectively.

**Quantitative Structure Determination. Layer Stacking Sequence of the 3R Samples.** In agreement with previous reports,<sup>57</sup> RoomT-KBi sample was indexed with a three-layer rhombohedral (3R) unit cell in space group  $R\bar{3}m$ . However, two distinct structure models match these requirements. Using the close-packing formalism, these idealized models are described as



where A, B, and C represent the positions of layer oxygen atoms ( $\text{O}_{\text{layer}}$ ), a, b, and c the positions of the layer Mn cations ( $\text{Mn}_{\text{layer}}$ ), and a', b', and c' the positions of interlayer K cations. In the first model (3R<sup>-</sup> polytype), adjacent layers are shifted with respect to each other by  $-a/3$  along the **a**

axis, thus leading to the prismatic coordination of interlayer species. In the second model (3R<sup>+</sup> polytype), adjacent layers are shifted with respect to each other by  $+a/3$  along the **a** axis, interlayer species being then octahedrally coordinated. For the two polytypes, diffraction lines have identical positions but differ by their relative intensities. The intensity of the  $20l$  ( $l = 3n + 1$ ) reflections is indeed much lower than that of  $11l$  ( $l = 3n - 1$ ) reflections for the 3R<sup>-</sup> polytype, whereas the  $20l$  reflections of the 3R<sup>+</sup> polytype are more intense than the  $11l$  ones (Figure 5a). The total intensity calculated for overlapped  $31l$  and  $02l$  ( $l = 3n$ ) reflections are similar for the two stacking modes. From the comparison of their experimental XRD patterns (Figure 3) with those calculated for the two polytypes, RoomT-KBi and all heated samples clearly correspond to the 3R<sup>-</sup> polytype, their layers being systematically shifted with respect to each other by  $-a/3$  along the **a** axis.

**Sample RoomT-KBi.** In the initial structure model,  $\text{Mn}_{\text{layer}}$  was located at the origin of the unit cell, and  $\text{O}_{\text{layer}}$  had coordinates (0.333, 0,  $\pm 0.046$ ) to match the 2.00 Å layer thickness previously reported for phyllosulfates.<sup>70,75–79,83,84</sup> In agreement with the proposed structural formula (eq 2), it was initially assumed that 0.924 Mn cations are present per layer octahedron. According to Chen et al.,<sup>57</sup> both interlayer K<sup>+</sup> cations and H<sub>2</sub>O molecules are located on the faces of the trigonal prisms formed by  $\text{O}_{\text{layer}}$  from adjacent layers (Figure 6, Position 1). For high-temperature K-birnessite with a similar layer octahedral composition, Gaillot et al. proposed

(83) Post, J. E.; Veblen, D. R. *Am. Mineral.* **1990**, *75*, 477–489.

(84) Gaillot, A.-C.; Drits, V. A.; Lanson, B.; Manceau, A. *Chem. Mater.* **2005**, in preparation.

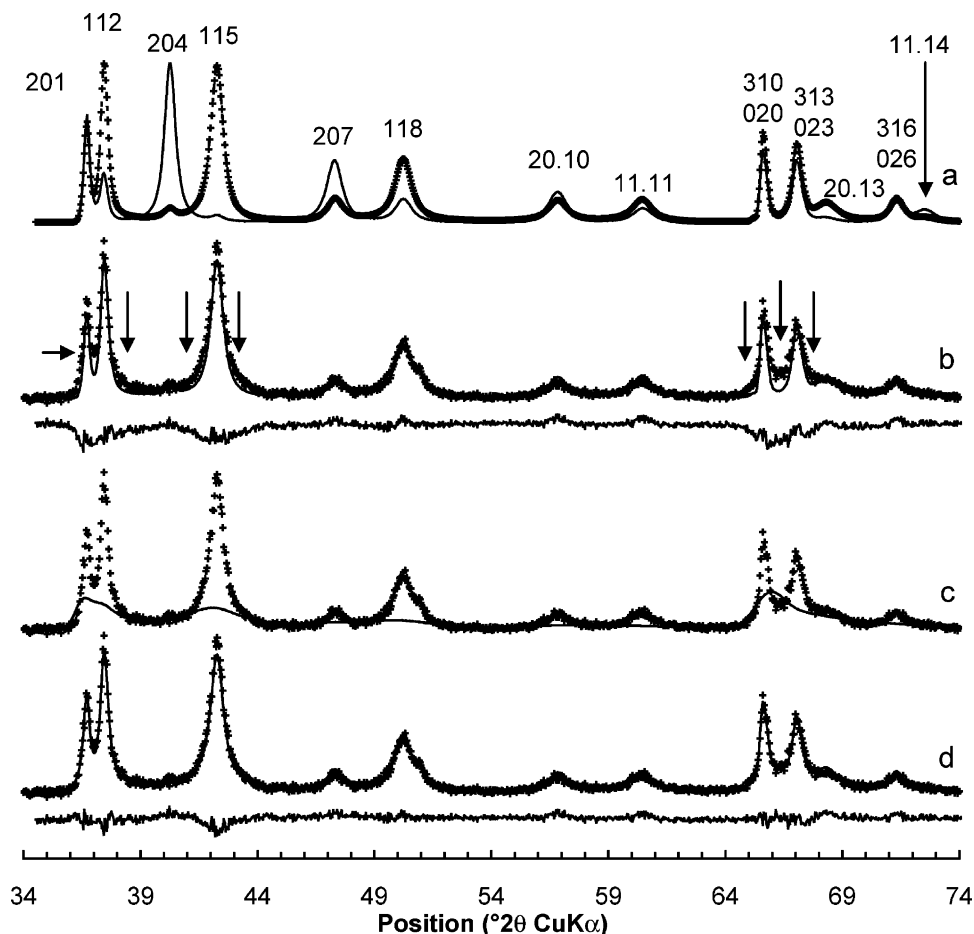


**Figure 5.** (a) Comparison of calculated XRD patterns corresponding to the  $3R^+$  (solid line) and  $3R^-$  (crosses) polytypes. (b) to (d) Comparison between experimental (crosses) and calculated (solid line) XRD patterns for sample RoomT-KBi. (b) Calculation performed assuming a periodic  $3R^-$  polytype ( $R_{wp} = 15.77\%$ ). Arrows indicate the misfits at peak tails. (c) Calculation performed assuming a quasi-turbostratic phase with small coherent scattering domain size. (d) Optimum model. The calculated pattern is the sum of the periodic  $3R^-$  polytype and of the quasi-turbostratic phase ( $R_{wp} = 9.55\%$ ).

an alternative position in the center of the interlayer prismatic cavity (Figure 6, Position 2).<sup>70</sup> In this alternative position, K is located above (or below) the empty tridentate cavity of the lower (or upper) layer and below (or above) a vacant or occupied Mn octahedron of the upper (or lower) layer. The intensity distributions calculated for  $20l$  and  $11l$  reflections assuming either model are compared in Figure 7a to the experimental XRD patterns of KBi samples. In both cases, calculated and experimental XRD patterns are similar and the solution does not appear univocal. Contrastingly, the intensity distribution of  $31l$  and  $02l$  reflections is extremely sensitive to the atomic coordinates of interlayer species. Specifically, after normalization of the calculated  $310/020$  maximum to the experimental one, the calculated  $313/023$  reflection is significantly lower than the experimental one when  $K^+$  is located in the center of the trigonal prisms and higher when  $K^+$  is located in the prism's faces (Figure 7b). The intensity ratio between these two diffraction maxima can thus be used to constrain the position of interlayer  $K^+$  cations, and the XRD simulations has thus been performed over the  $34\text{--}74^\circ$   $2\theta$  range for all KBi samples to include  $31l$  and  $02l$  reflections along with  $20l$  and  $11l$  ones. The best fit to the experimental XRD pattern (Figure 7b) was obtained when within each interlayer prism the site of  $K^+$  is split,  $K^+$  being shifted from the center of the prism toward its faces [Figure 6, Position 3;  $(-0.24, 0, 0.167)$ ]. A similar

position for interlayer  $K^+$  cations site was refined for high-temperature KBi samples with a similar layer octahedral composition.<sup>70</sup> In the optimum structure model for sample RoomT-KBi,  $H_2O$  molecules were located in the center of the interlayer space shifted from the edges of the trigonal prisms toward their centers, in six positions equivalent to  $(0.5, 0, 0.167)$  (Position 4, Figure 6). The interatomic distance between these  $H_2O$  molecules and the nearest  $O_{\text{layer}}$  from adjacent layers ( $O_{\text{layer}}\text{--}H_2O = 2.707 \text{ \AA}$  with a  $O_{\text{layer}}\text{--}H_2O\text{--}O_{\text{layer}}$  angle equal to  $144.7^\circ$ ) allows the formation of strong H-bonds which contribute significantly to the cohesion between layers.

However, when only the above phase is considered, a significant misfit to the experimental XRD pattern is visible at the tails of each diffraction maximum (Figure 5b,  $R_{wp} = 15.77\%$ ). This misfit was assumed to result from the presence in sample RoomT-KBi of an additional fine-grained phase whose structure is identical to that of the main phase but exhibiting a high structural disorder. The contribution of this very disordered phase (Figure 5c) has been included in all simulations to improve fit quality. This phase possibly corresponds to the material holding KBi crystals together and sometimes forming a "crust" over the ball-like aggregates (Figure 1b). Accordingly, the best fit to the RoomT-KBi experimental data (Figure 5d,  $R_{wp} = 8.90\%$ ) was obtained for a physical mixture (70:30 ratio) of a well-crystallized

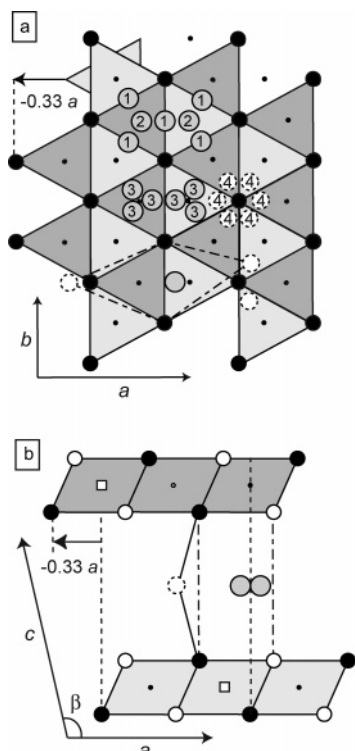


**Figure 6.** Structure model for the 3R<sup>-</sup> polytype. (a) Projection on the *ab* plane. The upper surface of the lower layer is shown as light shaded triangles whereas the lower surface of the upper layer is shown as dark shaded triangles. Mn<sub>layer</sub> and O<sub>layer</sub> of the two layers are shown as small and big solid circles, respectively. Large shaded circles represent interlayer K<sup>+</sup>. Position 1 corresponds to the faces of the interlayer prism defined by two empty tridentate layer cavities, whereas position 2 corresponds to the center of this prism. Position 3 corresponds to the optimum model. Open circles with a dashed outline (position 4) represent H<sub>2</sub>O molecules. Dot-dashed lines outline the coordination polyhedron of interlayer K<sup>+</sup> cations which includes 4 O<sub>layer</sub> and 2 H<sub>2</sub>O molecules. (b) Projection along the *b* axis. Open and solid symbols indicate atoms at  $y = 0$  and  $y = \pm 1/2$ , respectively. Large circles represent O<sub>layer</sub> atoms, small circles represent Mn<sub>layer</sub> atoms, and squares represent vacant layer octahedra. Dot-dashed lines outline the interlayer prisms defined by two empty tridentate layer cavities. The center of these prisms is shown by regular dashed lines. Other patterns as in Figure 6a.

3R<sup>-</sup> phase containing 5% of random stacking faults ( $W_R$ ) and of a quasi-turbostratic phase ( $W_R \sim 75\%$ ) having a smaller coherent scattering domain size (CSDS) in the *ab* plane (70 Å vs 300 Å). In the quasi-turbostratic phase, adjacent layers with a well-defined stacking mode are shifted with respect to each other by  $-a/3$  along the *a* axis. Although present in small proportion in the main 3R<sup>-</sup> phase ( $W_R = 5\%$ ), random stacking faults significantly increase the width of 20*l*/11*l* reflections with increasing *l* index (data not shown). This peak broadening, together with the presence of the poorly crystalline phase, impaired the use of conventional structure refinement techniques, including the Rietveld technique. As a consequence, the structural characterization of KBi samples was performed with the trial-and-error method described by Drits et al.<sup>74</sup> Atomic coordinates, site occupancies, and other structural parameters used to obtain the best possible agreement between experimental and calculated XRD patterns are listed in Table 3 whereas selected interatomic distances are reported in Table 4.

**Sample 100-KBi.** The main structural features of 100-KBi XRD pattern are essentially unchanged, as compared to that of RoomT-KBi. Interlayer water was assumed to be present

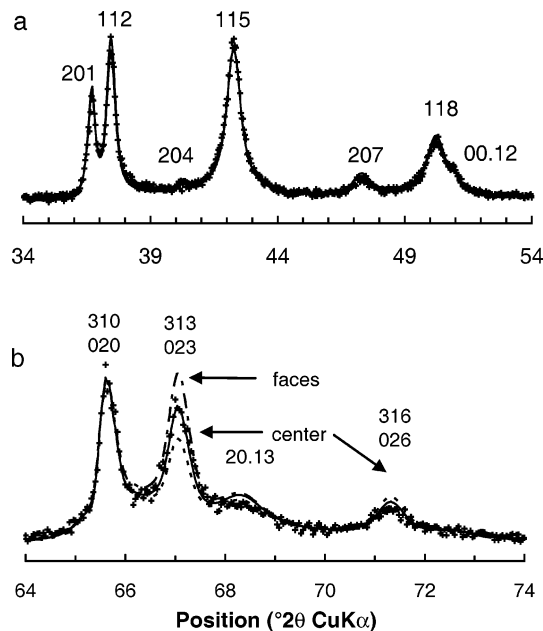


**Figure 7.** Comparison between experimental (crosses) and calculated (lines) XRD patterns for sample RoomT-KBi. Comparison is shown for 20*l*/11*l* reflections (a) and for 31*l*/02*l* ones (b). Dot-dashed and dashed lines correspond to calculations performed assuming interlayer K<sup>+</sup> cations on the faces (position 1 in Figure 6) or in the center (position 2 in Figure 6) of the interlayer prism, respectively. The solid line corresponds to the calculation performed with the optimum position of interlayer K<sup>+</sup> cations (position 3 in Figure 6).

in most interlayers, in agreement with the DT-TG data which indicates that only adsorbed H<sub>2</sub>O molecules were lost at 100 °C (first endothermic DT peak at ~90 °C) and with the limited decrease of the unit-cell *c* parameter. The structure model determined for sample RoomT-KBi was thus used as a starting point for calculation of XRD patterns, after adjusting unit-cell parameters to match the experimentally determined peak positions. The *x* coordinate of interlayer H<sub>2</sub>O molecules was changed (from 0.500 to 0.450, Table 3) to better match the experimental distribution of intensity (Figure 8a,  $R_{wp} = 18.59\%$ ). In addition, the degree of structural ordering and the crystallinity of KBi was found to be lower at 100 °C than at room temperature. The proportion of random stacking faults was indeed increased from 5 to 12% in the ordered structure, whereas its CSDS in the *ab* plane was decreased from 300 to 230 Å. The shoulder on the high-angle side of the 115 maximum which is visible on the 100-KBi experimental pattern (arrow, Figure 8a) was reproduced assuming the presence of a mixed-layer structure (MLS, Figure 8b). In this MLS, 30% of the layers are identical to the ones in the main ordered phase. The remaining 70% have the same layer structure but no interlayer water, and thus exhibit a lower unit-cell *c* parameter (Table 1, Figure 8b). Other structural parameters such as unit-cell *b* parameter, cation occupancy of the Mn<sub>layer</sub> site, and position of interlayer K<sup>+</sup> were identical to those determined for sample RoomT-KBi (Table 3). The partial dehydration observed in the accessory MLS is in agreement with the DT-TG results, and with the tailing of the 006 reflection toward high angles. The best fit to the experimental data (Figure 8c,  $R_{wp} = 12.24\%$ ) was obtained for a physical mixture of 77% of a fully hydrated periodic 3R<sup>-</sup> polytype, 8% of the accessory and partially dehydrated MLS, and 15%



Table 3. Atomic Positions, Sites Occupancies, and Other Structural Parameters in Hydrothermal KBi Samples

		RoomT-KBi	100-KBi	150-KBi	250-KBi	350-KBi		AfterT-KBi	
		3R <sup>-</sup>	3R <sup>-</sup>	3R <sup>-</sup>	3R <sup>-</sup>	A layer, 3R <sup>-</sup>	B layer, 3R <sup>+</sup>	3R <sup>-</sup>	1M <sup>a</sup>
Mn	$x^a$	0	0	0	0	0	0	0	0
	$y^a$	0	0	0	0	0	0	0	0
	$z^a$	0	0	0	0	0	0	0	0
	occ	0.925	0.925	0.925	0.925	1.000	1.000	1.000	1.000
O	$x^a$	±0.333	±0.333	±0.333	±0.333	±0.333	±0.333	±0.333	±0.341
	$y^a$	0	0	0	0	0	0	0	0
	$z^a$	±0.0465	±0.0473	±0.0516	±0.0519	±0.0516	±0.0516	±0.0473	±0.143
	$\zeta^b$	±1.00	±1.00	±1.00	±1.00	±1.00	±1.00	±1.00	±1.00
	occ	2	2	2	2	2	2	2	2
K <sup>c</sup>	$x^a$	-0.240	-0.240	-0.270	-0.290	-0.300	-0.300	-0.24	-0.400
	$y^a$	0	0	0	0	0	0	0	0
	$z^a$	0.5	0.5	0.5	0.5	0.5	0.5	0.5	0.5
	$\zeta^b$	3.582	3.525	3.230	3.210	3.201	3.226	3.525	3.500
	occ	0.050 × 2	0.050 × 2	0.050 × 2	0.050 × 2	0.050 × 2	0.050 × 2	0.050 × 2	0.150 × 2
K <sup>c</sup>	$x^a$	0.120	0.120	0.135	0.145	0.150	0.150	0.120	-
	$y^a$	±0.360	±0.360	±0.405	±0.435	±0.450	±0.450	±0.360	-
	$z^a$	0.5	0.5	0.5	0.5	0.5	0.5	0.5	-
	$\zeta^b$	3.582	3.525	3.230	3.210	3.201	3.226	3.525	-
	occ	0.050 × 4	0.050 × 4	0.050 × 4	0.050 × 4	0.050 × 4	0.050 × 4	0.050 × 4	-
H <sub>2</sub> O <sup>c</sup>	$x^a$	0.500	0.450					0.500	-0.4500
	$y^a$	0	0					0	0
	$z^a$	0.167	0.0167					0.167	0.5
	$\zeta^b$	3.582	3.525					3.525	3.500
	occ	0.070 × 2	0.070 × 2					0.060 × 2	0.190 × 2
H <sub>2</sub> O <sup>c</sup>	$x^a$	-0.250	-0.225					-0.250	
	$y^a$	±0.750	±0.675					±0.750	
	$z^a$	0.167	0.0167					0.167	
	$\zeta^b$	3.582	3.525					3.525	
	occ	0.070 × 4	0.070 × 4					0.060 × 4	
$N^d$	6/30	6/30	6/30	6/30	6/30	6/30		6/30	
$W_R^e$	5%	10–12%	12%	17%	10%	30%		30%	
CSD <sup>f</sup>	350	230	230	180	230	200		250	

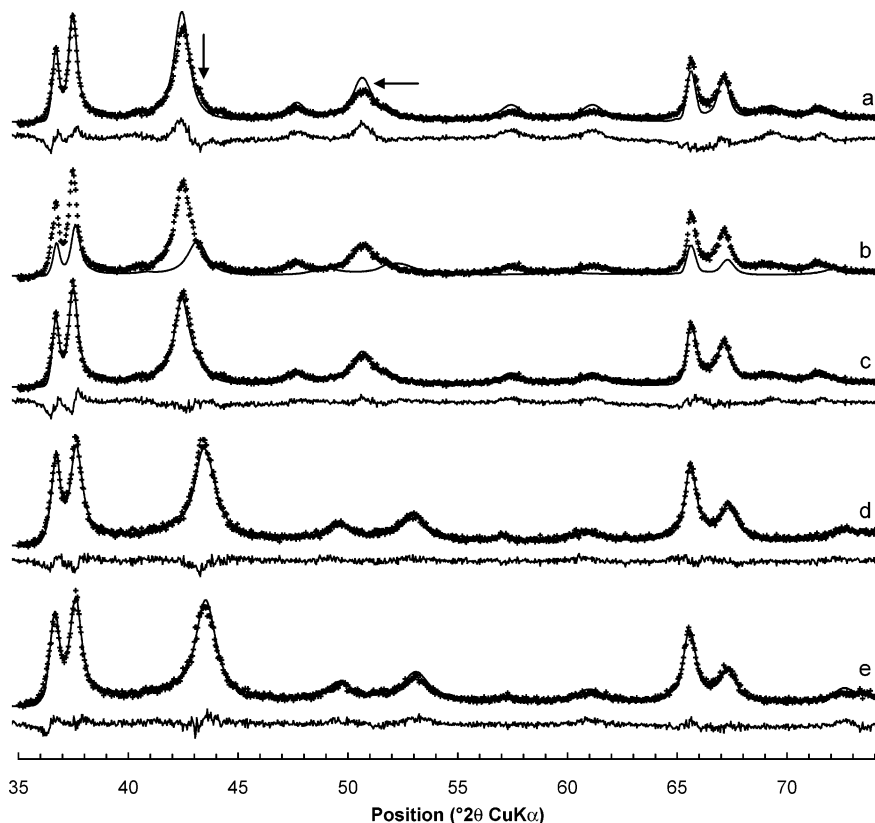
<sup>a</sup>  $x$ ,  $y$ , and  $z$  atomic positions are expressed in fraction of unit-cell  $a$ ,  $b$ , and  $c$  parameters.  $x$  positions are given in projection normal to the **ab** plane. <sup>b</sup> Position  $\zeta$  along  $c$  is expressed in Å to emphasize the thickness of layer and interlayer polyhedra. <sup>c</sup> For K and H<sub>2</sub>O only 3 of the 6 equivalent sites are reported. Additional sites are obtained by the symmetry operation  $x = -x$  and  $z = -z$ . <sup>d</sup> The extension of the coherent scattering domains perpendicular to the layer plane is expressed in number of layers  $N$  (mean/average). <sup>e</sup>  $W_R$  is the occurrence probability of random stacking faults for the well-crystallized phases. <sup>f</sup> CSD is the radius of the coherent scattering domains in the **ab** plane. For the quasi-turbostratic phase present in all samples,  $W_R = 75\%$  and CSDS = 70 Å. The values of Debye–Waller thermal factor ( $B$ ) are 0.5, 1.0, 2.0, and 2.0 for Mn<sub>layer</sub>, O<sub>layer</sub>, K<sub>interlayer</sub>, and H<sub>2</sub>O<sub>interlayer</sub>, respectively.

Table 4. Selected Interatomic Distances (in Å) in Hydrothermal KBi Samples

		RoomT-KBi	100-KBi	150-KBi	250-KBi	350-KBi		AfterT-KBi	
		3R <sup>-</sup>	3R <sup>-</sup>	3R <sup>-</sup>	3R <sup>-</sup>	3R <sup>-</sup>	3R <sup>+</sup>	3R <sup>-</sup>	1M
height of Mn layer		2.000	2.000	2.000	2.000	2.000	2.000	2.000	2.000
Mn <sub>layer</sub> –Mn <sub>layer</sub>	×6	2.845	2.845	2.850	2.851	2.868	2.885	2.870	2.934 × 2 2.850 × 4
Mn <sub>layer</sub> –O <sub>layer</sub>	×6	1.923	1.923	1.924	1.927	1.935	1.943	1.935	1.923 × 4 2.015 × 2
height of interlayer		5.164	5.040	4.460	4.420	4.402	4.452	5.050	5.000
K–O <sub>layer</sub> short	×4	2.970	2.917	2.696	2.709	2.708	2.734	2.928	2.703 × 1
K <sub>interlayer</sub> –O <sub>layer</sub> long	×2	3.330	3.282	2.968	2.855	2.855	2.881	3.298	2.831 × 1
average K <sub>interlayer</sub> –O <sub>layer</sub>	×6	3.090	3.039	2.787	2.758	2.757	2.783	3.051	2.767 × 2
K <sub>interlayer</sub> –H <sub>2</sub> O <sub>interlayer</sub>	×1	2.924	2.922					2.949	2.713 × 2
	×2	3.222	3.222					3.251	2.862 × 2 3.161 × 2
O <sub>layer</sub> –H <sub>2</sub> O <sub>interlayer</sub>	×2	2.705	2.650					2.658	2.616 × 1 2.720 × 1
O–H <sub>2</sub> O–O angle		144.71°	143.90°					143.67°	139.56°

of a poorly crystalline phase exhibiting a quasi-turbostratic stacking ( $W_R \sim 75\%$ ) and a small CSDS in the **ab** plane (70 Å). Structural parameters characterizing the optimal model for hydrated layers and selected interatomic distances are listed in Tables 3 and 4, respectively. Parameters of the dehydrated layers are similar to those determined for sample 150-KBi and reported in Table 3.

*Sample 150-KBi.* DT-TG results show that at 150 °C KBi dehydration is complete as the endotherm maximum was obtained at ~140 °C. Accordingly, the XRD pattern reveals a much smaller periodicity along the  $c^*$  direction ( $d(003) = 6.494$  Å), leading to a strong decrease of the unit-cell  $c$  parameter. Simultaneously, the unit-cell  $b$  parameter is slightly enlarged, most likely as the result of an increased



**Figure 8.** Comparison between experimental (crosses) and calculated (solid line) XRD patterns for KBi samples. (a) Sample 100-KBi. Calculation performed for a periodic hydrated  $3R^-$  polytype ( $R_{wp} = 18.59\%$ ). (b) Sample 100-KBi. Calculation performed for a mixed-layer structure in which 70% of the layers are dehydrated. (c) Sample 100-KBi. Optimum model. The calculated pattern is the sum of a periodic hydrated  $3R^-$  polytype, of a mixed-layer structure in which 70% of the layers are dehydrated and of a quasi-turbostratic phase ( $R_{wp} = 12.24\%$ ). (d) Sample 150-KBi. Optimum model. The calculated pattern is the sum of a periodic dehydrated  $3R^-$  polytype and of a quasi-turbostratic phase ( $R_{wp} = 8.92\%$ ). (e) Sample 250-KBi. Optimum model. The calculated pattern is the sum of a periodic dehydrated  $3R^-$  polytype and of a quasi-turbostratic phase ( $R_{wp} = 9.97\%$ ).

thermal motion and/or to better accommodate the presence of  $K^+$  cations in dehydrated interlayers. Apart from the shift of diffraction lines due to the collapse of KBi layers, the experimental XRD pattern of sample 150-KBi looks essentially similar to those obtained at lower temperatures, indicating that the structure of KBi is essentially unaffected by the dehydration. Consistently, in the optimum structure model  $K^+$  cations were located at the interlayer mid-plane and shifted toward the faces of the prismatic cavities in 6 positions equivalent to  $(-0.27, 0, 0.167)$ , although  $H_2O$  molecules were no longer present in the interlayer space. Note that this structure model is very similar to that determined for the dehydrated layers present in sample 100-KBi. The two models differ from each other only by the lateral unit-cell dimensions and interlayer  $K^+$  cations positions (Tables 1 and 3). The best fit to the experimental data (Figure 8d,  $R_{wp} = 8.92\%$ ) was obtained for a physical mixture of 61% of a well-crystallized phase ( $W_R = 10\%$ , CSDS in the  $ab$  plane =  $230 \text{ \AA}$ ) and 39% of a quasi-turbostratic phase ( $W_R \sim 75\%$ , CSDS =  $70 \text{ \AA}$ ). Structural parameters characterizing the optimal model and selected interatomic distances are listed in Tables 3 and 4, respectively.

**Sample 250-KBi Model.** The structure model determined for sample 250-KBi is also similar to the ones described above, although both the degree of structural ordering and the crystallinity keep degrading. The main ordered phase contains indeed 17% of random stacking faults, its average

CSDS in the  $ab$  plane being  $180 \text{ \AA}$ . The relative proportion of the quasi-turbostratic phase providing the best fit to the experimental data (Figure 8e,  $R_{wp} = 9.97\%$ ) is 25%. Structural parameters characterizing the optimal model and selected interatomic distances are listed in Tables 3 and 4, respectively.

**Sample 350-KBi.** The structure can be described to a large extent as a  $3R^-$  polytype, but significant structural changes are visible on the XRD pattern of 350-KBi (Figure 3e). In particular, the shoulder on the low-angle side of the 006 maximum (inset in Figure 3e) suggests the presence of layers with an interlayer spacing larger than that of the main phase. In addition, there is a strong increase of the unit-cell  $b$  parameter from  $2.845\text{--}2.851 \text{ \AA}$  ( $25\text{--}250 \text{ }^\circ\text{C}$ ) to  $2.868 \text{ \AA}$  at  $350 \text{ }^\circ\text{C}$  (Table 1, Figure 4), although layer symmetry remains hexagonal. This abrupt and dramatic increase cannot result solely from thermal motion as the unit-cell dilatation usually depends linearly on the temperature if the structure or the electronic state (for redox-sensitive elements) is not modified. Rather, it is likely that at this temperature  $Mn^{4+}$  was partially reduced to  $Mn^{3+}$ . As a result,  $\langle Mn-O \rangle$  distance was increased and lateral dimensions of the unit cell were enlarged to accommodate this augmentation.  $\langle Mn-O \rangle$  increases indeed from  $1.912 \text{ \AA}$  for  $Mn^{4+}$  (determined for  $\lambda\text{-MnO}_2$ )<sup>85</sup> to  $2.04 \text{ \AA}$  for  $Mn^{3+}$  in crednerite and other Mn-

(85) Thackeray, M. M.; de Kock, A.; David, W. I. F. *Mater. Res. Bull.* **1993**, *28*, 1041–1049.

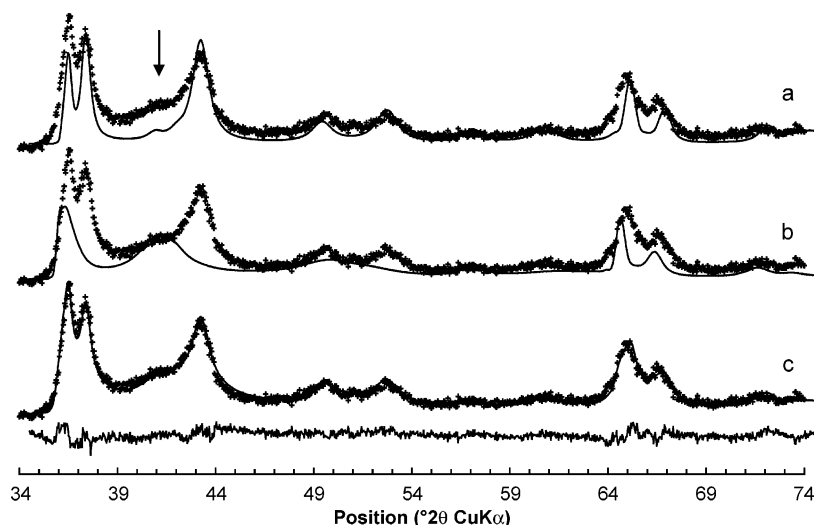


**Figure 9.** Comparison between experimental (crosses) and calculated (solid line) XRD patterns for sample 350-KBi. (a) Calculation performed for a periodic  $3R^-$  polytype. (b) Calculation performed for a mixed-layer structure containing 30% of layers shifted by  $-a/3$  along the  $\mathbf{a}$  axis ( $3R^-$  fragments) and 70% of layers shifted by  $+a/3$  along the  $\mathbf{a}$  axis ( $3R^+$  fragments). (c) Optimum model. The calculated pattern is the sum of a quasi-periodic  $3R^-$  structure of the above  $3R^-/3R^+$  mixed-layer structure, and of a quasi-turbostratic structure ( $R_{wp} = 9.92\%$ ).

oxyhydroxides.<sup>86–90</sup> As a consequence of the presence of trivalent  $Mn_{\text{layer}}$ , the layer charge deficit was assumed to derive essentially from the coexistence of heterovalent  $Mn_{\text{layer}}$  cations within the octahedral layer and no Mn vacant sites were considered in the structure model of 350-KBi (see structural formula, eq 3). Apart from the occupancy of the  $Mn_{\text{layer}}$  site, atomic coordinates and occupancies of the various sites were considered to be identical to those determined for sample 250-KBi. The resulting  $3R^-$  structure allowed reproducing the main features of the experimental diffraction pattern, except for the strong shoulder on the low-angle side of the 115 reflection which is visible only for sample 350-KBi (arrow in Figure 9a). The position of this shoulder is close to that of the 204 reflection of  $3R$  varieties, this reflection being extremely weak for the  $3R^-$  polytype but strong for the  $3R^+$  polytype (Figure 5a). Layers stacked with a  $+a/3$  interlayer displacement along the  $\mathbf{a}$  axis ( $3R^+$  polytype) are thus likely present in sample 350-KBi. Since the 204 maximum appears as a broad shoulder tailing toward the 115 reflection of the  $3R^-$  polytype, it is likely that  $3R^+$  and  $3R^-$  structural fragments coexist within the same crystallites. The diffraction effects resulting from the interstratification of  $3R^+$  and  $3R^-$  structural fragments within the same crystallites may be predicted from the considerations developed by Drits and co-workers.<sup>75,91,92</sup> By applying Méring's approach, which was developed initially for 00/ reflections, to  $hkl$  reflections, Drits and co-workers were able to demonstrate that the diffraction maxima observed for the MLS resulting from the random interstratification of fragments of periodic structures having similar layer structure

but different interlayer displacements are located between the maxima corresponding to the individual periodic structures. The actual position and intensity of these reflections depend on the proportion of each type of the interstratified fragments.<sup>91–93</sup> As for clay minerals,<sup>91</sup> this type of structural defect is common in birnessite.<sup>70,76,78,79</sup> In agreement with the above considerations, the 204 shoulder at  $\sim 41.5^\circ 2\theta$  in the 350-KBi XRD pattern was thus reproduced (Figure 9b) with the contribution of a MLS containing 30% of layers shifted by  $-a/3$  along the  $\mathbf{a}$  axis (A layers, corresponding to fragments of a  $3R^-$  polytype) and 70% of layers shifted by  $+a/3$  along the  $\mathbf{a}$  axis (B layers, corresponding to fragments of a  $3R^+$  polytype). The two layer types were randomly interstratified, and they both had unit-cell parameters  $a = 4.997 \text{ \AA}$  and  $b = 2.885 \text{ \AA}$ . The interlayer configuration within B fragments ( $3R^+$  polytype) is different from that in the A fragments because of the different layer stacking mode. In the former fragments, interlayer  $K^+$  cations have an octahedral rather than prismatic coordination and were found to be located in position  $(-0.3, 0, 0.167)$  (Figure 10). With respect to a given layer, this position of interlayer  $K^+$ , above and below the empty tridentate cavity of adjacent octahedral layers, is similar to that in the A layers.

The best fit to the experimental XRD pattern (Figure 9c,  $R_{wp} = 9.92\%$ ) was obtained for a physical mixture of quasi-periodic  $3R^-$  crystals (95:5 ratio between A and B layers, respectively,  $W_R = 10\%$ ), a  $3R^-/3R^+$  MLS (30:70 ratio between A and B layers, respectively,  $W_R = 30\%$ ), and a quasi-turbostratic structure ( $W_R = 75\%$ ,  $3R^-$  ordered layer stacking) in a 40:20:40 ratio. The CSDS in the  $\mathbf{ab}$  plane is slightly larger for 350-KBi crystals as compared to 250-KBi crystals (230  $\text{\AA}$  and 200  $\text{\AA}$  for the quasi-periodic  $3R^-$  structure and the MLS, respectively, as compared to 180  $\text{\AA}$ ).

*Sample AfterT-KBi.* XRD patterns of KBi recorded at room temperature before and after the thermal treatment differ strikingly (Figures 3a and 3f). Specifically, whereas the RoomT-KBi sample was dominated by a  $3R^-$  periodic

(86) Töpfer, J.; Trari, M.; Gravereau, P.; Chaminade, J. P.; Doumerc, J. P. *Z. Kristallogr.* **1995**, *210*, 184–187.

(87) Shannon, R. D.; Gummert, P. S.; Chenavas, J. *Am. Mineral.* **1975**, *60*, 714–716.

(88) Glasser, L. S. D.; Ingram, L. *Acta Crystallogr.* **1968**, *B24*, 1233–1236.

(89) Dachs, H. *Z. Kristallogr.* **1963**, *118*, 303–326.

(90) Norrestam, R. *Acta Chem. Scand.* **1967**, *21*, 2871–2884.

(91) Drits, V. A.; McCarty, D. K. *Am. Mineral.* **1996**, *81*, 852–863.

(92) Drits, V. A.; Varaxina, T. V.; Sakharov, B. A.; Plançon, A. *Clays Clay Miner.* **1994**, *42*, 382–390.

(93) Méring, J. *Acta Crystallogr.* **1949**, *2*, 371–377.

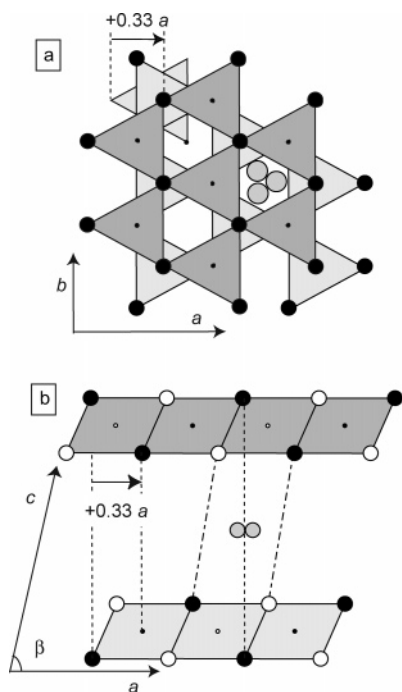


**Figure 10.** Structure model for the  $3R^+$  polytype. (a) Projection on the  $ab$  plane. (b) Projection along the  $b$  axis. Patterns as in Figure 6.

structure, simulation of its XRD patterns showed that sample AfterT-KBi consisted of two phases present in equal proportions. In one of the phases 90% of the layers are stacked according to a monoclinic  $1M$  structure. These layers are interstratified with layers forming  $3R^-$  structural fragments (Figure 11a,  $R_{wp} = 23.03\%$ ). The layers forming the  $1M$  and  $3R^-$  subsequences are partially incommensurate.  $1M$  layers exhibit an orthogonal layer symmetry with unit-cell parameters  $a_{ort} = 5.130 \text{ \AA}$ ,  $b_{ort} = 2.850 \text{ \AA}$  ( $a_{ort} > b_{ort}\sqrt{3}$ ),  $c = 7.131 \text{ \AA}$ ,  $\beta = 101.0^\circ$ ,  $T_x = c \cos \beta = -0.260 a$ . Unit-cell parameters of the  $3R^-$  fragments present in sample AfterT-KBi ( $a_{ort} = b_{ort}\sqrt{3} = 4.971 \text{ \AA}$ ,  $b_{ort} = 2.870 \text{ \AA}$ ,  $c =$

$21.150 \text{ \AA}$ ) are considerably increased as compared to those reported for RoomT-KBi ( $a_{ort} = 4.923 \text{ \AA}$ ,  $b_{ort} = 2.845 \text{ \AA}$ ,  $c = 21.492 \text{ \AA}$ , Table 1, Figure 4). This increase is consistent with the structural formula proposed for this sample (eq 3), which indicates the presence of a significant proportion of  $Mn^{3+}$  cations in vacancy-free layers. As indicated by their orthogonal layer symmetry,  $1M$  layers also contain a significant proportion of  $Mn^{3+}$  cations in vacancy-free layers. In these latter layers, interlayer  $K^+$  cations and  $H_2O$  molecules are located in  $(-0.40, 0, 0.5)$  and  $(-0.45, 0, 0.5)$ , respectively (Figure 12, Tables 4 and 5). These positions are similar to the main undifferentiated ( $K, H_2O$ ) position found by Post and Veblen  $(-0.413, 0, 0.5)$ ,<sup>83</sup> provided that their  $x$  position is given in projection normal to the  $ab$  plane. As both types of interstratified layer fragments consist of vacancy-free layers and likely contain a similar proportion of  $Mn^{3+}$ , the origin of their incommensurability is to be sought in the orientation distribution of distorted  $Mn^{3+}$  layer octahedra (see Discussion). As a result of the thermal treatment and of the induced chemical and structural modifications, the  $1M/3R^-$  MLS contains a high proportion of random stacking faults ( $W_R = 25\%$ ) as compared to low-to-medium-temperature KBi samples ( $W_R = 5\text{--}17\%$  for RoomT-, 100-, 150-, and 250-KBi samples).

The second phase present in sample AfterT-KBi was poorly crystallized (CSDS in the  $ab$  plane =  $70 \text{ \AA}$ ) and possessed a quasi-turbostratic structure ( $W_R = 75\%$ ).  $3R^-$  and  $1M$  structural fragments coexist in a 4:1 ratio among layers having a well-defined stacking (random interstratification, Figure 11b). Both  $3R^-$  and  $1M$  layers are identical in the two phases (unit-cell parameters, coordinates, and occupancies of the different sites, Table 4), and it was assumed that randomly stacked layers had the same lateral dimensions as  $3R^-$  layers. The best fit to the experimental XRD pattern is shown in Figure 11c ( $R_{wp} = 8.67\%$ ). Structural parameters characterizing the optimal model for

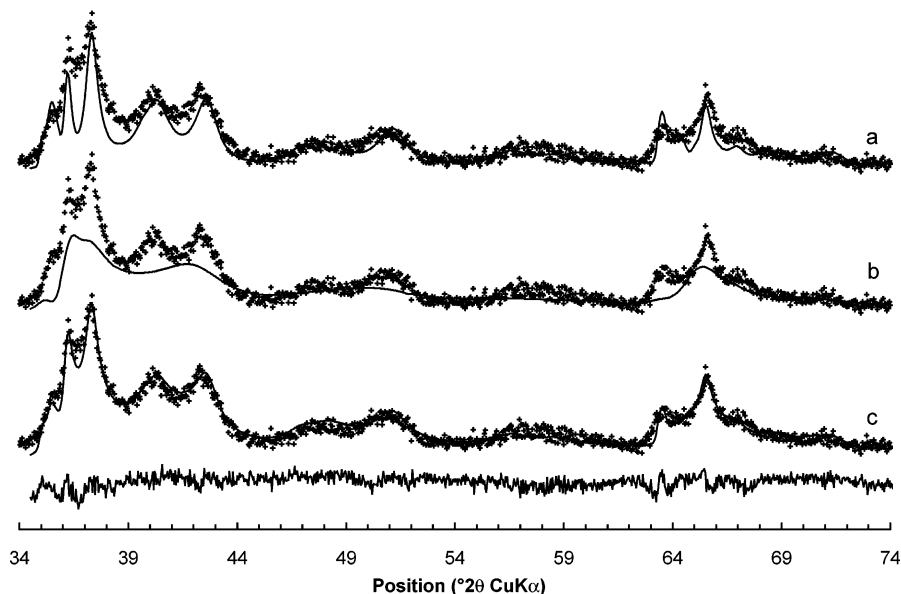


**Figure 11.** Comparison between experimental (crosses) and calculated (solid line) XRD patterns for sample AfterT-KBi. (a) Calculation performed for a mixed-layer structure containing  $1M$  and  $3R^-$  structural fragments (90:10 ratio,  $R_{wp} = 23.03\%$ ). (b) Calculation performed for a quasi-turbostratic phase containing  $3R^-$  and  $1M$  structural fragments. (c) Optimum model. The calculated pattern is the sum of the  $1M/3R^-$  mixed-layer structure and of the quasi-turbostratic structure described above ( $R_{wp} = 8.67\%$ ).

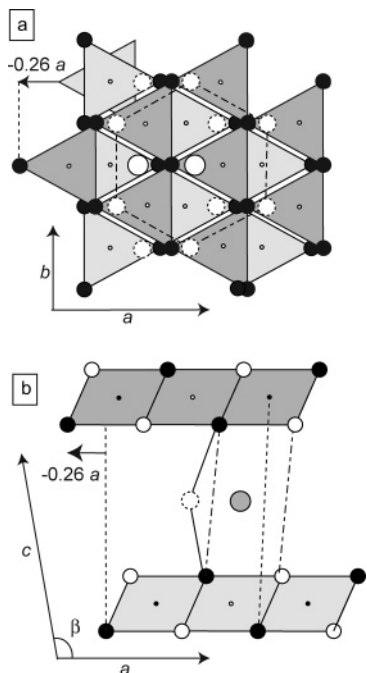


**Figure 12.** Structure model for the 1M polytype. (a) Projection on the *ab* plane. (b) Projection along the *b* axis. Patterns as in Figure 6.

both  $3R^-$  and 1M fragments and selected interatomic distances are listed in Tables 3 and 4, respectively.

### Discussion

The determination of structure models for all KBi samples allowed complementing our knowledge of crystal chemistry and structure of KBi obtained from the decomposition of  $\text{KMnO}_4$  under mild hydrothermal conditions and of their modifications upon temperature increase. In the following, the origin of the layer charge will be determined in the original sample and as a function of temperature along with structural changes. In particular, the partial reduction of  $\text{Mn}_{\text{layer}}$  and the migration of vacant sites within layer, which is associated with the departure of  $\text{O}_{\text{layer}}$ , will be discussed. Finally, the location of interlayer species will be analyzed as a function of temperature from its influence on layer structure stability.

**Crystal Chemistry of Sample RoomT-KBi.** *Cation Composition and Layer Structure.* Titration of Mn oxidation degree shows that the Mn oxidation state is reduced from +VII to +IV when KBi is obtained from the hydrothermal decomposition of  $\text{KMnO}_4$  and that no  $\text{Mn}^{3+}$  is formed. To the best of our present knowledge, this protocol is actually the only abiotic one that allows obtaining synthetic birnessite crystals exhibiting a three-dimensional ordering and containing only  $\text{Mn}^{4+}$  cations, which seems to be an important feature for electrochemical applications.<sup>69</sup> From the reduction of  $\text{KMnO}_4$  by  $\text{MnCl}_2$  in near neutral conditions Villalobos et al. also synthesized a birnessite sample ( $\delta\text{-MnO}_2$ ) containing only  $\text{Mn}^{4+}$  cations in the octahedral layers, but this birnessite was totally turbostratic ( $W_R = 100\%$ ) and presented extremely limited development of the layers in the *ab* plane.<sup>94</sup>

In agreement with the sole presence of  $\text{Mn}^{4+}$  cations within octahedral layers, individual and average Mn–O distances are equal to 1.92 Å ( $\pm 0.01$ ) in RoomT-KBi. This value is indeed typical for  $\text{MnO}_2$  compounds.<sup>87</sup> For example, similar (Mn–O) distances were reported in the  $\text{Mn}^{3+}$ -free layers of chalcophanite (1.923 Å) and of  $\lambda\text{-MnO}_2$  (1.912 Å).<sup>85,95</sup> As a consequence, KBi layers likely contain  $\sim 7\%$  of vacant octahedra which represent the sole source of layer charge deficit, in agreement with the proposed structural formula (eq 2). The layer cation composition and the source of layer charge deficit in hydrothermal KBi are thus similar to those observed for the sample  $\text{KBi}_8$  obtained from the thermal decomposition of  $\text{KMnO}_4$  at 800 °C whose  $\text{Mn}^{3+}$ -free layers contain 12% of vacant octahedra.<sup>70</sup> As in other phyllosilicates, octahedra building up KBi layers are flattened along the *c*\* axis as a result of the electrostatic repulsion between adjacent  $\text{Mn}_{\text{layer}}$ . The length of shared O–O edges in RoomT-KBi crystals (2.59 Å) is thus shorter than that of O–O edges on the basal surfaces of the crystals (2.84 Å, Table 4).

*Interlayer Structure.* Interlayer  $\text{K}^+$  cations occupy one of the six positions equivalent to the  $(-0.24, 0, 0.167)$  site (Position 3, Figure 6a). Each site in the interlayer mid-plane is shifted from one face of the prism toward its center. Interlayer  $\text{K}^+$  cations are coordinated by four  $\text{O}_{\text{layer}}$  atoms at  $\sim 2.970$  Å. Two  $\text{H}_2\text{O}$  molecules at 2.924 Å and 3.222 Å complete their first coordination shell. These short  $\text{K}-\text{O}_{\text{layer}}$  bond lengths significantly contribute to the cohesion between adjacent layers, together with short  $\text{H}_2\text{O}-\text{O}_{\text{layer}}$  distances (2.705 Å) which allow for strong H-bonds. The shift of interlayer  $\text{K}^+$  cations from the center of the prism decreases unfavorable electrostatic repulsion with the nearest  $\text{Mn}_{\text{layer}}$ . The position determined for interlayer  $\text{K}^+$  cations in RoomT-KBi is similar to that refined on a  $\text{KBi}_8$  monocrystal in which average  $\text{K}-\text{O}$  distances were also compatible with a 6-fold coordination ( $4\text{O}_{\text{layer}}$  and  $2\text{H}_2\text{O}$ ).<sup>70</sup>

In contrast to sample  $\text{KBi}_8$ , interlayers of RoomT-KBi are devoid of  $\text{Mn}^{3+}$  cations and the layer charge deficit is compensated for by the sole presence of 0.30 interlayer  $\text{K}^+$  cations. To provide local charge compensation, these cations should be close to the source of layer charge deficit. Specifically,  $\text{O}_{\text{layer}}$  coordinated to 2  $\text{Mn}_{\text{layer}}$  and a vacant layer site are strongly undersaturated, ideally receiving only  $2 \times 0.667 = 1.333$  vu (valence unit). Therefore, the location and distribution of  $\text{K}^+$  cations is most likely related to the distribution of vacant sites so as to provide local charge compensation. The absence of super-reflections in both XRD and selected-area electron diffraction patterns (data not shown) suggest that vacant sites and associated interlayer  $\text{K}^+$  cations are randomly distributed in KBi.

**Crystal Chemistry of KBi from 100 to 250 °C.** DT-TG results show, in agreement with XRD, that dehydration of KBi layers initiates at  $\sim 90$  °C and is complete at  $\sim 150$  °C. Apart from the departure of the interlayer  $\text{H}_2\text{O}$  molecules, which leads to the collapse of KBi layers, heating of KBi up to 250 °C does not alter its basic structure, which can be indexed in the  $R\bar{3}m$  space group ( $3R^-$  polytype) over this

(94) Villalobos, M.; Lanson, B.; Manceau, A.; Toner, B.; Sposito, G. *Am. Mineral.* **2005**, submitted.

(95) Post, J. E.; Appleman, D. E. *Am. Mineral.* **1988**, *73*, 1401–1404.

temperature range. The hexagonal symmetry of KBi layers is thus preserved and only a minor increase of unit-cell dimensions is observed, most likely as a result of thermal motion (Table 1, Figure 4). Once H<sub>2</sub>O molecules have left the structure, the 6-fold coordination of K<sup>+</sup> is likely ensured by the nearest six O<sub>layer</sub> defining the interlayer prismatic cavity. As a result of the dehydration, interlayer K<sup>+</sup> cations thus slightly migrate from (−0.24, 0, 0.167) at room temperature toward the center of the prism at 250 °C [(−0.29, 0, 0.167), Table 3] most likely to provide more appropriate K–O<sub>layer</sub> distances after the partial layer collapse. In addition, the relative proportion of random stacking faults (*W<sub>R</sub>*) steadily increases (from 5 to 17%) with increasing temperature in the well-crystallized phases, whereas the CSDS in the **ab** plane is decreasing from 300 Å to 180 Å. In contrast, the CSDS along the **c\*** axis in the well-crystallized phases remains unchanged with temperature (6 layers on average) and the relative proportion of the fine-grained quasi-turbostratic phase does not vary significantly with temperature (Table 3).

**Structure Modification of KBi at 350 °C.** Whereas KBi structure is stable up to 250 °C, significant chemical and structural modifications occur when temperature reaches 350 °C. Specifically, modifications affecting unit-cell dimensions, Mn oxidation state, and related weight loss reported in the Results section will be discussed below.

*Evolution of Layer Dimensions and Mn Oxidation State.* The temperature increase from 250 °C to 350 °C does not modify the layer symmetry. However, a significant increase of the layer unit-cell parameters is observed from *b* = 2.851 Å at 250 °C to *b* = 2.868 Å and 2.885 Å for the layers of the 3R<sup>−</sup> phase and of the MLS, respectively. A significant weight loss (2.7 wt %, Figure 2) also accompanies the temperature increase. As mentioned above, such dramatic increase of the unit-cell dimensions within the **ab** plane is likely not related to thermal motion but rather to the partial reduction of Mn<sup>4+</sup> to Mn<sup>3+</sup>. Chemical analysis of KBi crystals after cooling indeed revealed a much lower Mn mean oxidation state (3.78 for sample AfterT-KBi vs 4.00 for sample RoomT-KBi). Partial reduction from Mn<sup>4+</sup> to Mn<sup>3+</sup> most likely account for the observed decrease which is likely due to the presence of 22% of Mn<sup>3+</sup> cations in the heated sample. Herstein et al. also observed a weight loss (3.7 wt %) when heating a K<sub>0.5</sub>Mn<sub>0.875</sub>O<sub>2</sub> sample to ~500 °C and associated this effect with an oxygen loss, which was in turn hypothesized to result from the partial reduction of Mn<sup>4+</sup> to Mn<sup>3+</sup>.<sup>57,68</sup> Because ⟨Mn–O⟩ distances are longer for Mn<sup>3+</sup> (2.04 Å) than for Mn<sup>4+</sup> cations (1.912 Å), the presence of such a high amount of Mn<sup>3+</sup> in KBi layers is responsible for the significant increase of the unit-cell dimensions within the **ab** plane.

The hexagonal layer symmetry may at first sight seem to contradict the presence of Mn<sup>3+</sup> cations in the layer. Mn<sup>3+</sup> cations are known indeed to be affected by the Jahn–Teller effect that lowers the symmetry of the 3d electron orbitals and distorts the octahedra leading to 4 short and 2 long Mn–O distances. To minimize the resulting steric strains in Mn<sup>3+</sup>-rich birnessites, Mn<sup>3+</sup>-octahedra distorted by the Jahn–Teller effect are commonly segregated in Mn<sup>3+</sup>-rich rows

parallel to the **b** axis and are systematically oriented with their long Mn–O bonds (2.26 Å in crednerite)<sup>86</sup> along the **a** axis, giving rise to an orthogonal layer symmetry. This cooperative Jahn–Teller effect was reported for Na- and Ca-birnessite varieties obtained from the oxidation of Mn<sup>2+</sup>,<sup>75,77,96</sup> and for a K-birnessite variety obtained from reduction of Mn<sup>7+</sup> at 1000 °C.<sup>84</sup> In the absence of cooperative Jahn–Teller effect the long Mn–O bonds of Mn<sup>3+</sup> octahedra are randomly oriented at ±*n*120° (*n* integer) with respect to the **a** axis. In this case, the hexagonal symmetry of the layers is preserved, but the resulting increase of the average octahedron size increases the unit-cell *b* parameter as compared to phyllosilicates that are devoid of Mn<sup>3+</sup> cations. Such a hexagonal layer symmetry with large unit-cell *b* parameter (2.925 Å) has been reported for lithiophorite whose layers contain 33% of Mn<sup>3+</sup> octahedra.<sup>95</sup>

For sample 350-KBi, the unfavorable presence of strains in the layers is likely compensated for by the thermal energy available at 350 °C. The proposed model is supported by the experimental results obtained by Gaillot et al. for a KBi sample obtained from the thermal decomposition of KMnO<sub>4</sub> at 1000 °C (KBi<sub>100</sub>).<sup>84</sup> This sample has a Mn<sub>0.737</sub><sup>4+</sup>Mn<sub>0.246</sub><sup>3+</sup>□<sub>0.017</sub> layer cation composition, orthogonal layer symmetry with *a* = 5.155 Å, *b* = 2.846 Å, *a/b* = 1.811, and exhibits an ordered distribution of Mn<sup>3+</sup>- and Mn<sup>4+</sup>-octahedra in its layers. The layer symmetry of KBi<sub>100</sub> sample becomes hexagonal with an increase of the unit-cell *b* parameter to 2.895 Å when heated in situ to 350 °C, in relation to the redistribution of distorted Mn<sup>3+</sup>-octahedra orientations at ±*n*120° (*n* integer) with respect to the **a** axis with equal probability for all three possible values of *n*. The abrupt increase of the unit-cell parameter *b* for sample 350-KBi can thus be considered as additional evidence for the presence of a significant amount of Mn<sup>3+</sup> octahedra in 350-KBi layers, and for the partial reduction of Mn<sup>4+</sup> to Mn<sup>3+</sup> at 350 °C.

*Loss of Weight and Associated Structural Transformation of the Layer (Loss of O<sub>layer</sub> and Migration of Vacant Layer Sites).* Together with the formation of layer Mn<sup>3+</sup> cations and with the associated increase of the unit-cell *a* and *b* parameters, the temperature increase up to 350 °C induces a 2.7% weight loss over the 250–400 °C range. This weight loss likely results from the migration of vacant layer octahedra and from the induced formation of vacancy-free layers. A significant temperature increase can indeed allow the migration of Mn<sub>layer</sub> to the nearest vacant sites forming new vacant sites. Consistently, sample AfterT-KBi, whose layers are essentially devoid of vacant sites, exhibits a weight gain rather than a weight loss over the 250–400 °C range (Figure 2b). A similar process of cation migration within octahedral layers has been described for example in 2:1 phyllosilicates. During the dehydroxylation of Fe<sup>3+</sup>- and Mg<sup>2+</sup>-rich dioctahedral micas, which occurs at ~450–600 °C, octahedral Fe<sup>3+</sup> and Mg<sup>2+</sup> cations migrate within the layer to the adjacent vacant octahedron to restore the structure stability which was disturbed following dehydroxylation.<sup>97–99</sup> Cation migration has also been de-

(96) Drits, V. A.; Silvester, E. J.; Gorshkov, A. I.; Manceau, A. *Am. Mineral.* **1997**, *82*, 946–961.

scribed when octahedral  $\text{Fe}^{3+}$  is reduced in 2:1 phyllosilicates.<sup>24</sup> In KBi layers, cation migration may result either in the migration of vacant sites to crystal edges or in the formation of vacancy clusters. In both cases, migration of vacant layer sites results in the reduction of the amount of vacant layer sites and in the loss of  $\text{O}_{\text{layer}}$ .

Loss of  $\text{O}_{\text{layer}}$  was shown to occur during the thermal reduction of synthetic pyrolusite ( $\text{MnO}_2$ ) in situ between 300 °C and 500 °C.<sup>82</sup> Using electron energy loss spectroscopy analysis, these authors were able to follow the reduction of Mn as a function of temperature by simultaneously determining the valence state of Mn and quantifying the relative proportion of oxygen vacancies created. In their study, Wang et al. found that reduction of  $\text{MnO}_2$  occurs between 300 °C and 400 °C with no visible structural change. However, they identified a “valence state conversion from 4+ to mixed valence state  $\text{Mn}^{4+}$ ,  $\text{Mn}^{3+}$ , and  $\text{Mn}^{2+}$ ” associated with a decrease of the O/Mn ratio from 2.00 to  $\sim 1.64$  (values taken from Figure 4 in Wang et al.).<sup>82</sup> For our KBi sample, the extent of  $\text{O}_{\text{layer}}$  loss can be estimated theoretically from the modification of KBi structural formula induced by the heating. Transformation from sample Room-KBi (structural formula  $\text{K}_{0.30}^+(\text{Mn}_{0.925}^{4+}\square_{0.075})\text{O}_2$ , eq 2) to sample 350-KBi leads to a  $\text{K}_{0.30}^+(\text{Mn}_{0.625}^{4+}\text{Mn}_{0.300}^{3+})\text{O}_{1.85}$  structural formula for the latter vacancy-free layers. As a result the theoretical weight loss associated with the departure of  $\text{O}_{\text{layer}}$  is  $\sim 2.5$  wt %, in agreement with that experimentally determined (2.7 wt %). The structural formula proposed for the vacancy-free layers of sample 350-KBi can thus be transformed to  $\text{K}_{0.324}^+(\text{Mn}_{0.676}^{4+}\text{Mn}_{0.324}^{3+})\text{O}_2$ . A similar agreement between calculated (4.0%) and experimentally determined (3.7%) weight loss corresponding to the departure of  $\text{O}_{\text{layer}}$  is obtained for the sample studied by Herbstein et al. using the structural formulas reported for their initial ( $\text{K}_{0.50}^+(\text{Mn}_{0.875}^{4+}\square_{0.125})\text{O}_2$ ) and heat-treated ( $\text{K}_{0.50}^+(\text{Mn}_{0.375}^{4+}\text{Mn}_{0.50}^{3+})\text{O}_{1.75}$ ) specimens.<sup>68</sup>

In conclusion, the weight loss observed over the 250–400 °C temperature range for synthetic birnessites may be considered as evidence for the presence of vacant layer sites in the sample at room temperature. In the present case, the weight loss results from the thermally induced migration of the vacant sites from the structure to the edges of the layers, thus inducing their vanishing and the associated loss of  $\text{O}_{\text{layer}}$ . Note that over the same temperature range weight loss can be alternatively related to the dehydroxylation of birnessite, as described for high-temperature KBi obtained at 800 °C.<sup>70</sup> In this case, the weight loss results from the departure of  $\text{OH}^-$  groups initially bonded to pre-existing  $\text{Mn}^{3+}$  cations located in the interlayer region, above or below the layer vacant sites, rather than in the octahedral layer.

**Layer Stacking Mode and Interlayer Structure.** In addition to the above structural modifications, heating of KBi sample from 250 °C to 350 °C is accompanied by a strong decrease of structural order and by a modification of the layer stacking

for part of the layers. Simulation of 350-KBi XRD pattern shows indeed that the main well-crystallized phase keeps the initial  $3R^-$  stacking sequence in which adjacent layers are shifted with respect to each other by  $-a/3$  along the **a** axis. In contrast, in the accessory MLS phase 70% of the layers (B layers) are shifted by  $+a/3$  along the **a** axis ( $3R^+$  stacking sequence). These layers are randomly interstratified with layers that kept their initial  $3R^-$  polytype (A layers). This layer stacking modification is likely related to the increased amount of  $\text{Mn}^{3+}$  in the octahedral layers and to the associated decreased amount of vacant layer sites. At room temperature, half of the interlayer  $\text{K}^+$  cations are most likely located above the empty tridentate cavity of the lower layer and below a vacant octahedral site of the upper one (or vice versa,  $\text{AbC}_b^a\text{CaB}\dots$  stacking sequence, Figure 6). At 350 °C, the proportion of vacant layer sites is strongly decreased and in A layers interlayer  $\text{K}^+$  cations are systematically facing an occupied Mn octahedron on one side of the interlayer. The resulting  $\text{K}-\text{Mn}$  repulsion could destabilize the layer stacking. By contrast, the initial prismatic coordination of interlayer  $\text{K}^+$  observed in A layers is modified in B layers to become octahedral ( $\text{AbC}_b^a\text{A}^c\text{BcA}\dots$ , Figure 10). The latter coordination seems more favorable as interlayer  $\text{K}^+$  cations are located above and below empty tridentate cavities of the two adjacent layers, the  $\text{K}-\text{Mn}$  repulsion being then screened by  $\text{O}_{\text{layer}}$ . This interlayer configuration would allow a higher content of layer  $\text{Mn}^{3+}$  and a lower vacant site content in layers of  $3R^+$  fragments, and would explain the larger unit-cell parameters of the layers in the accessory MLS as compared to those of layers making up the  $3R^-$  main phase ( $b = 2.885$  Å and 2.868 Å, respectively).

**Degree of Crystallinity and Structural Order of 350-KBi.** The CSDS within the **ab** plane of both the main  $3R^-$  phase and of the MLS are slightly increased as compared to that of the main 250-KBi phase (200–230 Å vs 180 Å, respectively, Table 3). This difference is likely due to the dramatic rearrangement of layer cations resulting from the partial reduction of  $\text{Mn}^{4+}$  to  $\text{Mn}^{3+}$  and from the subsequent migration of vacant layer octahedra. On the other hand, the proportion of random stacking faults is very high in the main well-crystallized  $3R^-$  phase ( $W_R = 30\%$ ), most likely as the result of the unfavorable direct repulsion between interlayer  $\text{K}^+$  cations and  $\text{Mn}_{\text{layer}}$  ones induced by the evolution of KBi crystal chemistry occurring at this temperature.

**Structural Transformation of 350-KBi into AfterT-KBi.** Comparison of the phase composition and structure in 350-KBi and AfterT-KBi samples allows proposing a structural mechanism for the phase transformation occurring when sample 350-KBi is cooled to obtain sample AfterT-KBi. Indeed, the relative proportion of the main well-crystallized  $3R^-$  phase in sample 350-KBi (40%) is similar to that of the proportion of the  $1M/3R^-$  MLS in sample AfterT-KBi (50%). To ease the following discussion, dehydrated  $3R^-$  polytype in sample 350-KBi and hydrated  $3R^-$  polytype in sample AfterT-KBi will be hereafter referred to as  $3R^-_d$  and  $3R^-_h$ , respectively. It is likely that during this transition the  $3R^-_d$  is transformed into the  $1M$  structure (with 10% residual  $3R^-_h$ ) whereas the accessory  $3R^+_d/3R^-_d$  MLS (ratio 70:30)

(97) Muller, F.; Drits, V. A.; Plancon, A.; Besson, G. *Clay Miner.* **2000**, *35*, 491–504.

(98) Muller, F.; Drits, V. A.; Tsipursky, S. I.; Plancon, A. *Clay Miner.* **2000**, *35*, 505–514.

(99) Muller, F.; Drits, V.; Plancon, A.; Robert, J. L. *Clays Clay Miner.* **2000**, *48*, 572–585.

from sample 350-KBi will contribute to the quasi-turbostratic phase which contains  $3R^-_h$  and  $1M$  fragments (4:1 ratio) in sample AfterT-KBi.

*Origin of 1M Layers.* Because of its prevalence, the transition from the  $3R^-_d$  polytype to the  $1M$  polytype will be considered first. As mentioned above, the new-formed  $Mn^{3+}$ -octahedra in the  $3R^-_d$  structure have a random orientation of their long  $Mn^{3+}-O$  bonds relative to the  $\mathbf{a}$  axis ( $\pm n120^\circ$ ), thus inducing significant lattice strains in the layers. Besides, interlayer  $K^+$  cations are shifted toward the center of interlayer prismatic cavities to ensure proper bond lengths with closest  $O_{\text{layer}}$  from adjacent layers. This shift, along with the absence of vacant layer sites and the interlayer collapse due to dehydration, significantly increase the repulsion between interlayer  $K^+$  and  $Mn_{\text{layer}}$ . At 350 °C, the effect of these structural features unfavorable to layer stability is compensated for by thermal energy. Logically, when lowering the temperature, stabilization of the resulting  $1M$  structure will ideally lead to the minimization of lattice strains and  $K^+-Mn_{\text{layer}}$  interactions. In addition, rehydration of  $1M$  interlayers should be accompanied by the formation of appropriate  $K^+-H_2O$  and  $H_2O-O_{\text{layer}}$  bond lengths so as to provide local charge compensation and to contribute to the cohesion between adjacent layers. These different aspects of AfterT-KBi structure will be discussed hereafter for the main  $1M/3R^-_h$  phase.

From chemical analysis, sample AfterT-KBi contains ~22% of the  $Mn^{3+}$  (structural formula, eq 3), and both the orthogonal symmetry of the layers in the  $1M$  polytype (Table 1) and the structure model determined (Table 3) suggest that these cations are actually located in the octahedral layer. The presence of a significant amount of  $Mn^{3+}$  cations in vacancy-free layers indeed leads, at room temperature, to the departure from the hexagonal layer symmetry because of cooperative Jahn–Teller effect. The transformation of  $3R^-_d$  polytype to  $1M$  polytype is most likely accompanied by such reorientation of the layer  $Mn^{3+}$ -octahedra, leading to a unique orientation of the long  $Mn^{3+}-O$  bonds and thus giving rise to the orthogonal layer symmetry. Such systematic orientation along the  $\mathbf{a}$  axis of the long  $Mn^{3+}-O$  bonds of distorted octahedra minimizes strains in the layers as the four short  $Mn^{3+}-O$  distances are similar to  $\langle Mn^{4+}-O \rangle$  (1.93 Å vs 1.91 Å). For this reason unit-cell  $b$  parameters are very similar (2.84–2.86 Å) in all  $Mn^{3+}$ -rich natural and synthetic varieties having orthogonal layer symmetry regardless of their layer  $Mn^{3+}$  content.<sup>69,75,77,83,84,96</sup> In contrast, the unit-cell  $a$  parameter strongly depends on this content and  $a/b$  ratios vary significantly for such  $Mn^{3+}$ -rich compounds. Values reported in the literature for  $a/b$  ratio are 1.936 in crednerite ( $CuMnO_2$ ,  $Mn^{3+} = 100\%$ ),<sup>86</sup> 1.830 in Na-buserite (NaBu,  $Mn^{3+} = 33\%$ ,  $a = 5.223$  Å,  $b = 2.854$  Å),<sup>75</sup> 1.817 Å in triclinic Na-birnessite (NaBi,  $Mn^{3+} = 30\%$ ,  $a = 5.174$  Å,  $b = 2.848$  Å),<sup>77,83</sup> and 1.811 in K-rich birnessite obtained from the thermal decomposition of  $KMnO_4$  at 1000 °C (KBi<sub>100</sub>,  $Mn^{3+} = 25\%$ ,  $a = 5.155$  Å,  $b = 2.846$  Å).<sup>84</sup> In  $1M$  layers of sample AfterT-KBi, unit-cell  $b$  parameter ( $b = 2.850$  Å) is consistent with literature data and  $a/b$  ratio equals 1.800, which would correspond to ~20% of  $Mn^{3+}$  in the layers. This value is consistent with

the average oxidation state of Mn measured globally for sample AfterT-KBi (22%).

Along with the reorientation of distorted layer  $Mn^{3+}$ -octahedra, the  $3R^-_d$ -to- $1M$  transformation during cooling is accompanied by modification of layer stacking, as the interlayer shift decreases from  $-0.333 a$  to  $-0.260 a$  ( $\Delta = +0.073 a$ ). As the average CSDS along the  $\mathbf{c}^*$  axis of both 350-KBi and AfterT-KBi samples is equal to 6 layers, maximum displacement between layers of a given crystal induced by the layer stacking modification does not exceed  $5\Delta$ , that is ~1.5 Å, taking into account the variation of unit-cell parameters. This displacement is likely even smaller as hydration of the  $3R^-_d$  interlayers during cooling most likely starts simultaneously from both ends of the crystals. These limited layers displacements are likely to require little energy to proceed.

In addition, mutual arrangement of layers in the  $1M$  polytype is favorable to the layer stacking stability as it allows for the formation of H-bonds and for the minimization of cation electrostatic repulsion. Each interlayer  $K^+$  cation is indeed coordinated by the two nearest  $O_{\text{layer}}$  from adjacent layers (2.703–2.831 Å) and by four (or even six)  $H_2O$  molecules at 2.713–2.862 Å (and 3.161 Å).  $H_2O$  molecules are located at 2.616 Å from the nearest  $O_{\text{layer}}$ , thus forming strong H-bonds (Figure 12). Finally, as compared to the  $3R^-_h$  phase, the  $1M$  layer stacking leads to an increased K–Mn distance, thus decreasing the repulsion between these two cations (Figures 6 and 12).

Note that the main structural features of the  $1M$  phase are similar to those of the K-saturated birnessite synthesized at high pH and room temperature from  $Mn^{2+}$  precursors.<sup>83</sup> It is likely that  $3R^-_h$  layer fragments (10%) coexisting with the prevailing  $1M$  fragments are inherited from the initial  $3R^-_d$  structure of sample 350-KBi in which the random orientation of the layer  $Mn^{3+}$  octahedral is maintained.

*Origin of the  $3R^-_h$  Fragments in the Quasi-Turbostratic Phase.* At first sight the hypothesized transition from the  $3R^+_d/3R^-_d$  MLS into the poorly crystallized phase during cooling of sample 350-KBi appears unlikely as at least one of the stability unfavorable factors described for the  $3R^-_d$  polytype is absent in the  $3R^+_d$  one. In the  $3R^+_d$  phase each interlayer  $K^+$  cation is indeed octahedrally coordinated and located above/below empty tridentate cavities from the two neighboring layers (Figure 10). As a result, proper K– $O_{\text{layer}}$  bond lengths are obtained with closest  $O_{\text{layer}}$  from adjacent layers (Table 4), and direct interaction with the  $Mn_{\text{layer}}$  cations is avoided. After cooling of the  $3R^+_d/3R^-_d$ , adjacent layers in the hydrated phase could thus logically maintain the  $+a/3$  interlayer shift along the  $\mathbf{a}$  axis to preserve such favorable disposition of layer and interlayer cations. In addition, this layer stacking mode would allow for the formation of strong H-bonds between  $O_{\text{layer}}$  and  $H_2O$  molecules if the latter were located between  $O_{\text{layer}}$  of adjacent layers in a position equivalent to (0.167, 0, 0.167) (Figure 10). However, through H-bonds neutral  $H_2O$  molecules provide  $O_{\text{layer}}$  with positive charges and they should thus interact with interlayer cations to compensate for this transfer of charge. A careful analysis of the  $3R^+_h$  interlayer space shows that the location of  $K^+$  cations in the interlayer octahedral site is inconsistent with



positions of H<sub>2</sub>O molecules, allowing for H-bond formation, K–H<sub>2</sub>O distances being either too short or too long. As a consequence, hydration of the 3R<sup>+</sup><sub>d</sub> phase following the cooling of sample 350-KBi should involve a modification of the 3R<sup>+</sup> stacking so that two conditions are satisfied. First, H<sub>2</sub>O molecules should form H-bonds with adjacent O<sub>layer</sub> and interact with interlayer K<sup>+</sup> cations. Second, interlayer K<sup>+</sup> cations should have appropriate coordination and proper  $\langle \text{K}-\text{O}_{\text{layer}} \rangle$  bond length.

As discussed above, these two conditions are satisfied in the 1M phase. It is thus likely that 3R<sup>+</sup><sub>d</sub> fragments present in the 3R<sup>+</sup><sub>d</sub>/3R<sup>-</sup><sub>d</sub> MLS tend to transform into such 1M fragments. However, thermal energy is likely not sufficient to allow a complete modification of the layer stacking from  $+a/3$  to  $-0.260a$  and random stacking faults in the quasi-turbostratic phase most likely result from displacements between adjacent layers intermediate between these two values. Thermal energy is not sufficient either to modify the hexagonal layer symmetry which is preserved in the quasi-turbostratic phase despite the unfavorable lattice constraints resulting from the presence of layer Mn<sup>3+</sup> cations. Note also that the relative proportion of 3R<sup>-</sup><sub>h</sub> and 1M fragments in the quasi-turbostratic phase (20% and 5%, respectively) is similar to that of the 3R<sup>-</sup><sub>d</sub> fragments (30%), which have the “right” interlayer displacement, in the 3R<sup>+</sup><sub>d</sub>/3R<sup>-</sup><sub>d</sub> MLS in sample 350-KBi.

Interlayer structure of the 3R<sup>-</sup><sub>h</sub> phase in the KBi sample after cooling is similar to that determined before thermal treatment. In both cases, interlayer K<sup>+</sup> cations are coordinated

by four O<sub>layer</sub> defining the faces of the prism and by two H<sub>2</sub>O molecules located in the interlayer mid-plane. These H<sub>2</sub>O molecules have appropriate distances both with the nearest O<sub>layer</sub> from adjacent layers and with the nearest interlayer K<sup>+</sup> cations. The main difference between the 3R<sup>-</sup><sub>h</sub> phases in KBi samples before thermal treatment and after cooling arises from their respective layer cation composition. After cooling, layers of the 3R<sup>-</sup><sub>h</sub> phase are vacancy-free and interlayer K<sup>+</sup> cations are systematically located above or below Mn<sub>layer</sub>. As a result, 3R<sup>-</sup><sub>h</sub> structural fragments in the AfterT-KBi sample should be considered as metastable, although electrostatic repulsion between the two cations is partly decreased by the shift of the interlayer K<sup>+</sup> cations from the center of the prismatic cavity toward its faces. Metastability of these fragments also comes from the presence of lattice strains originating from the random orientation of distorted Mn<sup>3+</sup>-octahedra in the layers.

**Acknowledgment.** V.A.D. is grateful to the Environmental Geochemistry Group of the LGIT (Grenoble, France) and to the Russian Science Foundation for financial support. B.L. acknowledges financial support from INSU/Géomatériaux, and CNRS/PICS709 programs. The authors are grateful to Pr. Alain Plançon (IST – Orléans) for the availability and the modification of his XRD calculation program. Céline Boissard (Hydr’ASA – Poitiers), Martine Musso and Delphine Tisserand (LGIT – Grenoble), and Serge Nitsche (CRM-CN – Marseilles) are thanked for their technical support (DT-TG analyses, chemical analyses, and SEM images, respectively).

CM0500152